Pseudospectral methods with PML for nonlinear Klein-Gordon equations in classical and non-relativistic regimes

Xavier Antoine, Xiaofei Zhao

PSEUDOSPECTRAL METHODS WITH PML FOR NONLINEAR KLEIN-GORDON EQUATIONS IN CLASSICAL AND NON-RELATIVISTIC REGIMES

XAVIER ANTOINE AND XIAOFEI ZHAO

Abstract. Two different Perfectly Matched Layer (PML) formulations with efficient pseudo-spectral numerical schemes are derived for the standard and non-relativistic nonlinear Klein-Gordon equations (NKGE). A pseudo-spectral explicit exponential integrator scheme for a first-order formulation and a linearly implicit preconditioned finite-difference scheme for a second-order formulation are proposed and analyzed. To obtain a high spatial accuracy, new regularized Bermúdez type absorption profiles are introduced for the PML. It is shown that the two schemes are efficient, but the linearly implicit scheme should be preferred for accuracy purpose when used within the framework of pseudo-spectral methods combined with the regularized Bermúdez type functions. In addition, in the non-relativistic regime, numerical examples lead to the conclusion that the error related to regularized Bermúdez type absorption functions is insensitive to the small parameter ε involved in the NKGE. The paper ends by a two-dimensional example showing that the strategy extends to the rotating NKGE where the vortex dynamics is very well-reproduced.

Keywords: nonlinear Klein-Gordon equation, perfectly matched layer, absorption function, spectral accuracy, non-relativistic limit, pseudo-spectral method, exponential integrator

AMS Subject Classification: 81Q05, 80M22, 37M15

1. Introduction

The Klein-Gordon equation was originally proposed to describe the dynamics of spinless particles, and is known as the relativistic version of the Schrödinger equation. It has been widely applied in the studies of quantum field theory, cosmology and plasma physics [16, 26, 41, 42]. In this work, we consider the following d-dimensional ($d = 1, 2, 3$) nonlinear Klein-Gordon equation (NKGE) [15, 26, 34]:

$$\begin{cases} \dfrac{1}{c^2}\partial_{tt}u(\mathbf{x},t) - \Delta u(\mathbf{x},t) + \dfrac{m^2c^2}{\hbar^2}u(\mathbf{x},t) + \lambda|u(\mathbf{x},t)|^2u(\mathbf{x},t) = 0, \quad t > 0,\ \mathbf{x} \in \mathbb{R}^d, \\ u(\mathbf{x},0) = u_0(\mathbf{x}), \quad \partial_t u(\mathbf{x},0) = v_0(\mathbf{x}), \quad \mathbf{x} \in \mathbb{R}^d, \end{cases} \tag{1.1}$$

where $c > 0$ is the speed of light, $\hbar > 0$ denotes the Planck constant, $m > 0$ is the particle mass and $\lambda > 0$ is a given constant describing the strength of the defocusing interaction. In addition, the unknown function is $u = u(\mathbf{x}, t) : \mathbb{R}^d \times [0, \infty) \to \mathbb{C}$, where $u_0, v_0 : \mathbb{R}^d \to \mathbb{C}$ are two given initial data. Here, the global well-posedness of the defocusing NKGE (1.1) is guaranteed by [28], while for the focusing case $\lambda < 0$, there could be finite time blow-up [22]. The following energy or Hamiltonian of (1.1) is also conserved

$$H(t) := \int_{\mathbb{R}^d} \left[\frac{1}{c^2}|\partial_t u(\mathbf{x},t)|^2 + |\nabla u(\mathbf{x},t)|^2 + \frac{m^2c^2}{\hbar^2}|u(\mathbf{x},t)|^2 + \frac{\lambda}{2}|u(\mathbf{x},t)|^4 \right] d\mathbf{x} \equiv H(0), \quad t \geq 0. \tag{1.2}$$

Since the initial-value problem (1.1) is set in $\mathbb{R}^d$, the spatial domain has to be truncated to use a standard numerical discretization scheme, e.g. finite-difference, finite-element or pseudo-spectral scheme [15]. In the present paper, our aim is to apply the Fourier pseudo-spectral discretization scheme [38] which leads to highly accurate numerical solutions of PDEs with smooth coefficients and is widely used in computations of quantum mechanics [4, 5, 6, 7, 8, 11, 12, 13, 14, 15, 16, 27, 35]. As a consequence, one needs to impose periodic boundary conditions on the fictitious boundary delimiting the (rectangular) computational domain. Because of this constraint, any truncation technique based on non-reflecting/artificial/absorbing boundary condition for nonlinear PDEs [3, 9]

cannot be applied. Since its introduction in the seminal paper by Bérenger [18], the Perfectly Matched Layer (PML) approach provides an alternative powerful tool to simulate the numerical solution of PDEs in unbounded domains [1, 2, 3, 9, 10, 17, 19, 20, 21, 24, 25, 32, 43]. Concerning nonlinear PDEs, the PML technique has been applied for example to the nonlinear Schrödinger equations [3, 9, 10, 43], Euler and Navier-Stokes equations [31] or two-fluid plasma equations [40]. Concerning the nonlinear wave equations, Appelö and Kreiss [2] proposed and studied a first-order PML formulation with Dirichlet/Neumann boundary conditions related to Hagstrom techniques [1, 29]. In addition, some first numerical experiments were presented to analyze the potentiality of the approach which was also tested for the one-dimensional linear Klein-Gordon equation in [9] again using finite-differences. The aim of the present paper is to address the application and assessment of the PML approach to solve complex NKGE, both in the classical and non-relativistic regimes, considering Fourier pseudo-spectral approximation schemes.

In Section 2, we introduce the first-order PML formulation in the classical scaling, inspired by the works by Appelö and Kreiss in [2]. To obtain an explicit pseudo-spectral scheme, we use an exponential-wave integrator discretization. In addition, we also derive a second-order PML formulation of the NKGE, related to the standard developments for time-harmonic wave and Schrödinger equations. The discretization is now based on a Crank-Nicolson scheme combined with the pseudo-spectral method and an efficient preconditioned Krylov (GMRES) subspace iterative solver. This yields a linearly implicit scheme with a cost similar to the one for the explicit first-order PML formulation. Since we use a pseudo-spectral approach, the PDE with PML that has to be discretized requires some smooth coefficients but also some stability of the PML for the tuning parameters. To this end, we introduce some generalized singular Bermúdez-type absorption functions which are locally smoothed at the inner PML boundary. This allows us to achieve simultaneously a high (near-spectral) accuracy of the scheme and stable PML layers that are less sensitive to the tuning parameters, for the second-order formulation. The first-order PML formulation is shown to be less accurate and is not recommended in the pseudo-spectral framework. The conclusions are supported by a thorough numerical study. In Section 3, we extend and evaluate the numerical methods for the non-relativistic scaling. This shows that the second-order formulation combined with the pseudo-spectral scheme is again an efficient and accurate method for solving the NKGE, and most particularly thanks to the small ε parameter appearing in the non-relativistic regime. In Section 4, we extend the method to a two-dimensional rotating NKGE that models the dynamics of the cosmic superfluid set in a rotating frame [35, 42]. We show in particular that the numerical method in the bounded domain is able to simulate very accurately the dynamics of the vortices. Finally, we conclude in Section 5.

2. PML in classical scaling

To simplify the presentation, we first consider the one-dimensional real-valued case of the NKGE, i.e. $d = 1$, $\mathbf{x} = x$ and $u \in \mathbb{R}$ in (1.1), and we begin by looking at its classical dimensionless form [28, 36]:

$$\begin{cases} \partial_{tt} u(x,t) - \partial_{xx} u(x,t) + u(x,t) + \lambda u(x,t)^3 = 0, \quad t > 0,\ x \in \mathbb{R}, \\ u(x,0) = u_0(x), \quad \partial_t u(x,0) = v_0(x), \quad x \in \mathbb{R}. \end{cases} \tag{2.1}$$

Such classical scaling describes the physical system with wave speed at the same order of the speed of light. We shall consider two types of PML formulations for (2.1) in the sequel. One is a first-order formulation proposed by Appelö and Kreiss in [2] for general nonlinear wave equations, and the other one is a second-order analogy of the PML widely applied e.g. for nonlinear Schrödinger equations [9, 10, 43].

2.1. PML-I.

Let us begin by the modal ansatz construction with postulation

$$u(x,t) = \mathrm{e}^{kx+st} \mathrm{e}^{\frac{k}{s+\alpha} \int_0^x \sigma(\rho) d\rho}, \quad \partial_x \to \frac{s+\alpha}{s+\alpha+\sigma} \partial_x, \tag{2.2}$$

where $\sigma = \sigma(x) \geq 0$ is some chosen function known as the *absorption function*, s is interpreted as the variable in the Laplace-transform domain, and $\alpha \geq 0$ is a chosen parameter. By assuming that $\mathrm{Re}(s) \geq 0$ and $k \in \mathbb{C}$ in (2.2) satisfy the dispersion relation for the linear version of the model,

e.g. $\partial_{tt}u - \partial_{xx}u + u = 0$, a formulation of the PML equations as a first-order system has been proposed for a class of general nonlinear wave equations in [2]. Here, we can directly apply such PML formulation (called PML-I) to the NKGE (2.1), leading to

$$\begin{cases} \partial_{tt}u - \partial_{xx}u + u + \lambda u^3 = \sigma\left[\eta_2 - \partial_t u + \alpha u\right] + \partial_x(\sigma\eta_1), \quad t > 0,\ x \in I^*, \\ \partial_t\eta_1 + (\sigma+\alpha)\eta_1 + \partial_x u = 0, \\ \partial_t\eta_2 + \alpha\eta_2 + (\alpha^2+1)u + \lambda u^3 = 0, \\ u(x,0) = u_0(x), \quad \partial_t u(x,0) = v_0(x), \quad \eta_1(x,0) = \eta_2(x,0) = 0, \quad x \in I^*, \\ u(-L^*,t) = u(L^*,t), \quad \eta_1(-L^*,t) = \eta_1(L^*,t), \quad \eta_2(-L^*,t) = \eta_2(L^*,t), \quad t \geq 0, \end{cases} \tag{2.3}$$

where

$$I^* = (-L^*, L^*) \quad \text{with} \quad L^* = L + \delta$$

is a bounded interval for some $\delta > 0$, and $\eta_1 = \eta_1(x,t)$, $\eta_2 = \eta_2(x,t)$ are two auxiliary functions introduced in order to localize the layer equations in time. The initial conditions for the two auxiliary functions in (2.3) are suggested to be zero in [43].

The absorption function $\sigma(x)$ is required to satisfy

$$\sigma(x) = 0, \quad -L \leq x \leq L, \quad \text{and} \quad \sigma(x) > 0, \quad L < |x| \leq L^*,$$

such that inside the physical domain $[-L, L]$ the NKGE and its solution remain the same. The damping effect takes place only inside the layer, i.e. $L < |x| \leq L^*$. The smoothness of $\sigma(x)$ in the layer region $L \leq |x| \leq L^*$, particularly at the interface $|x| = L$, determines the regularity of the PML solution $u(x,t)$. When the NKGE (2.1) is linear ($\lambda = 0$), the absorbing layer (2.3) is perfectly matching [2]. Similar PMLs of the first-order formulation have also been derived for other hyperbolic systems [1, 32]. The boundary conditions for (2.3) at $|x| = L^*$ can be for example the homogeneous Dirichlet or Neumann boundary condition which were considered in [2]. In either case, the reflected waves at the boundary enter again the layer region and so are damped twice. Here we adopt periodic boundary conditions as suggested in [9, 10], so that the Fourier pseudo-spectral method [38] can be easily applied for the spatial discretization of the PML equations. Note that the periodicity of the boundary ensures that the waves hitting the outer boundary enter the layer from the other side of the domain which is the same as the 'round-way' damping.

Let us discuss briefly the damping effect brought by (2.2) for the Klein-Gordon equation and the choice of α. Firstly, we remark that with $\alpha = 0$, the damping effect

$$\frac{k}{s}\int_0^x \sigma(\rho)d\rho$$

in (2.2) is a typical choice for dispersionless materials, where the phase velocity k/s is constant so that all waves attenuate at the same rate [32]. For the PML-I formulation for the NKGE (2.3), we consider the linear case, i.e. $\lambda = 0$ in (2.1) or (2.3) to illustrate the damping effect. By taking the modal solution $u = \mathrm{e}^{kx+st}$, we have the dispersion relation for the original linear Klein-Gordon equation:

$$s^2 = k^2 - 1 \ \Rightarrow\ k = -\sqrt{s^2+1}, \tag{2.4}$$

and so (2.2) reads

$$u(x,t) = \mathrm{e}^{kx+st}\mathrm{e}^{-\frac{\sqrt{s^2+1}}{s+\alpha}\int_0^x \sigma(\rho)d\rho}.$$

This means that the modal solution e^{kx+st} for PML-I (2.3) is damped inside the layer $L < |x| \leq L^*$ by the absorption function σ modulated by the factor $g(s)$:

$$g(s) = -\frac{\sqrt{s^2+1}}{s+\alpha}, \quad \text{for} \quad \mathrm{Re}(s) > 0. \tag{2.5}$$

We show in Figure 1 the mapping of the right half plane of the complex domain $\mathrm{Re}(s) > 0$ under the function $g(s)$ for $\alpha = 0$ and $\alpha = 0.5$. We can see that for $\mathrm{Re}(s) > 0$ and $\alpha \geq 0$, we always have $\mathrm{Re}(g) < 0$. However, it is difficult to say if there exists or not an optimal choice of the shifting parameter α even for such a linear equation. The reason is that there could always be some $g(s)$ getting arbitrarily close to the imaginary axis for some s, with $\mathrm{Re}(s)$ arbitrarily small.

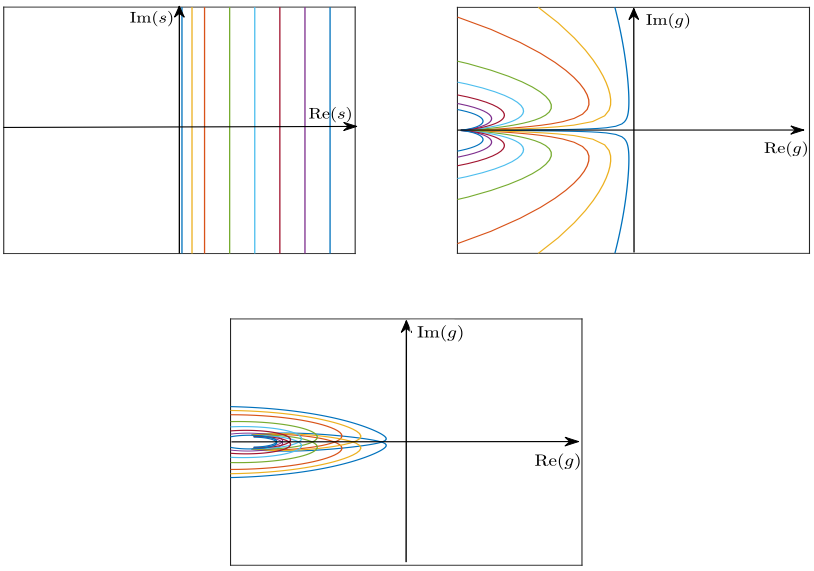

FIGURE 1. The right half complex plane $\mathrm{Re}(s) > 0$ (top left) under mapping $g = -\sqrt{s^2+1}/(s+\alpha)$: $\alpha = 0$ (top right) and $\alpha = 0.5$ (bottom).

To numerically solve the PML-I equations (2.3), instead of the finite difference time-domain discretization in [2], our periodic boundary setup in (2.3) is natural to apply the Fourier spectral discretization which is directly diagonalized in space, and we integrate in time under the framework of the exponential wave integrator [14, 27, 30]. Denoting $\tau = \Delta t > 0$ as the time step and $t_n = n\tau$ for $n \in \mathbb{N}$ as the discrete times, we shall derive in the following a fully explicit exponential wave integrator Fourier pseudo-spectral method for (2.3). For simplicity of notations, we will omit in the following the spatial variable x in a space-time dependent function, e.g. $u(t) = u(x,t)$. Let

$$v(t) := \partial_t u(t), \quad t \geq 0.$$

Then, by applying the Duhamel's formula to (2.3), we have

$$\begin{aligned}
u(t_{n+1}) =& \cos(\langle\partial_x\rangle\tau)u(t_n) + \frac{\sin(\langle\partial_x\rangle\tau)}{\langle\partial_x\rangle}v(t_n) + \int_0^\tau \frac{\sin(\langle\partial_x\rangle(\tau-\rho))}{\langle\partial_x\rangle}f(t_n+\rho)d\rho,\\
v(t_{n+1}) =& -\langle\partial_x\rangle\sin(\langle\partial_x\rangle\tau)u(t_n) + \cos(\langle\partial_x\rangle\tau)v(t_n) + \int_0^\tau \cos(\langle\partial_x\rangle(\tau-\rho))f(t_n+\rho)d\rho,\\
\eta_1(t_{n+1}) =& \mathrm{e}^{-(\sigma+\alpha)\tau}\eta_1(t_n) - \int_0^\tau \mathrm{e}^{(\sigma+\alpha)(\rho-\tau)}\partial_x u(t_n+\rho)d\rho,\\
\eta_2(t_{n+1}) =& \mathrm{e}^{-\alpha\tau}\eta_2(t_n) - \int_0^\tau \mathrm{e}^{\alpha(\rho-\tau)}\left[(\alpha^2+1)u(t_n+\rho) + \lambda u(t_n+\rho)^3\right]d\rho, \quad n \geq 0,\ x \in I^*,
\end{aligned}$$

where we set $\langle\partial_x\rangle = \sqrt{1-\partial_{xx}}$ and

$$f(t_n+\rho) := \sigma(\eta_2(t_n+\rho) - v(t_n+\rho) + \alpha u(t_n+\rho)) + \partial_x(\sigma\eta_1(t_n+\rho)) - \lambda u(t_n+\rho)^3.$$

Applying the trapezoidal rule to the above integrals, we obtain the following exponential-wave integrator Fourier pseudo-spectral (EWI-FP) scheme: by introducing $u^n \approx u(t_n), v^n \approx v(t_n), \eta_1^n \approx$

$\eta_1(t_n), \eta_2^n \approx \eta_2(t_n)$, for $n \geq 0$, we have

$$u^{n+1} = \cos(\langle\partial_x\rangle\tau)u^n + \frac{\sin(\langle\partial_x\rangle\tau)}{\langle\partial_x\rangle}v^n + \frac{\tau\sin(\langle\partial_x\rangle\tau)}{2\langle\partial_x\rangle}f^n, \tag{2.6a}$$

$$\eta_1^{n+1} = \mathrm{e}^{-(\sigma+\alpha)\tau}\eta_1^n - \frac{\tau}{2}\left[\mathrm{e}^{-(\sigma+\alpha)\tau}\partial_x u^n + \partial_x u^{n+1}\right], \tag{2.6b}$$

$$\eta_2^{n+1} = \mathrm{e}^{-\alpha\tau}\eta_2^n - \frac{\tau}{2}\left[\mathrm{e}^{-\alpha\tau}\left(\left(\alpha^2+1\right)u^n + \lambda(u^n)^3\right) + \left(\alpha^2+1\right)u^{n+1} + \lambda\left(u^{n+1}\right)^3\right], \tag{2.6c}$$

$$v^{n+1} = -\langle\partial_x\rangle\sin(\langle\partial_x\rangle\tau)u^n + \cos(\langle\partial_x\rangle\tau)v^n + \frac{\tau}{2}\left[\cos(\langle\partial_x\rangle\tau)f^n + f^{n+1}\right], \tag{2.6d}$$

with

$$f^n = \sigma\left(\eta_2^n - v^n + \alpha u^n\right) + \partial_x(\sigma\eta_1^n) - \lambda(u^n)^3.$$

Here, the scheme (2.6) and the numerical solution $(u^n, v^n, \eta_1^n, \eta_2^n)$ are defined on the spatial grids: $x_j = -L^* + jh$ for $j = 0, 1, \ldots, N-1$ with some even integer $N > 0$ and mesh size $h = 2L^*/N$.

The above EWI-FP scheme is fully explicit in time by computing (2.6a) to (2.6d). The involved spatial differentiation operators can all be implemented efficiently under Fourier pseudo-spectral method [38] by fast Fourier transform (FFT), resulting in a computational cost $O(N\log N)$. Concerning the stability of the EWI-FP scheme, noting the term $\partial_x u$ in (2.6b) and the term $\partial_x(\sigma\eta_1^n)$ appearing in (2.6a) and (2.6d), we have some unbalanced energy norms on both sides of (2.6). Therefore, we are expecting a CFL stability constraint:

$$\tau < Ch, \quad \text{for some} \quad C > 0.$$

For the accuracy, noticing the quadrature error from the trapezoidal rule and the interpolation error from the Fourier pseudo-spectral method, it can be analyzed similarly as in [14, 27] that the global error of the above EWI-FP method for (2.3) up to some finite time reads

$$O(\tau^2) + O(h^{m_0}),$$

for some $m_0 > 0$ which depends on the smoothness of the PML solution of (2.3). We shall show numerically that by using a very smooth absorption function $\sigma(x)$ particularly with high-order continuous derivatives at the interface point $|x| = L$, the EWI-FP could reach a spectral-like accuracy for spatial discretization. Thanks to the spectral accuracy, we can use a rather large $h > 0$ in practice so that the above CFL condition is not too restrictive.

2.2. **PML-II.** For dispersive models like the nonlinear Schrödinger equations (NSE), the phase velocity is naturally non-constant with respect to the wavelength. Therefore, instead of (2.2), an average damping effect has been widely considered in the postulation of a modal solution:

$$u(x,t) = \mathrm{e}^{kx+st}\mathrm{e}^{kR\int_0^x\sigma(\rho)d\rho}, \tag{2.7}$$

for some chosen $R \in \mathbb{C}$ as for the NSE. Using (2.7) for the NKGE (2.1), by directly changing

$$\partial_x \to \frac{1}{1+R\sigma}\partial_x,$$

we consider the following second PML formulation (PML-II):

$$\begin{cases} \partial_{tt}u - \dfrac{1}{1+R\sigma}\partial_x\left(\dfrac{1}{1+R\sigma}\partial_x u\right) + u + \lambda u^3 = 0, \quad t > 0,\ x \in I^*, \\ u(x,0) = u_0(x), \quad \partial_t u(x,0) = v_0(x), \quad x \in I^*, \\ u(-L^*,t) = u(L^*,t), \quad t \geq 0. \end{cases} \tag{2.8}$$

Here, we also impose the periodic boundary condition in (2.8) for the convenience of spatial discretization.

An obvious advantage of PML-II (2.8) over PML-I (2.3) is that PML-II does not require any auxiliary variables. We only need to solve one equation in (2.8), instead of three equations in (2.3). The PML-II can be considered as a second-order formulation, which is an analogy of the PML e.g. for NSE [9, 10, 43]. Note that for the NSE, the shifting parameter R is usually chosen as $R = \mathrm{e}^{i\pi/4}$ [43]. However, for the NKGE (2.8), this choice generates some instabilities, and we need to consider

$R > 0$. Indeed, assuming again $\lambda = 0$ in (2.1) with the modal solution $u = \mathrm{e}^{kx+st}$, by the dispersion relation (2.4), we have in (2.7):

$$u(x,t) = \mathrm{e}^{kx+st}\mathrm{e}^{-R\sqrt{s^2+1}\int_0^x \sigma(\rho)d\rho}.$$

Then in order to make the solution decay inside the layer, we ask for

$$\mathrm{Re}\left(-R\sqrt{s^2+1}\right) < 0, \quad \forall\, \mathrm{Re}(s) > 0.$$

We illustrate in Figure 2 the mapping $g(s) = -\sqrt{s^2+1}$ of the right half complex plane. It can be clearly seen that the choice of R for the PML (2.8) is restricted to a positive real number, otherwise any non-zero imaginary part of R leads to some $\mathrm{Re}\left(-R\sqrt{s^2+1}\right) > 0$ which triggers instability. This will be verified by numerical tests later. Since R must be positive, it can be viewed in (2.8) only as a modification of $\sigma_0 > 0$, namely the strength of the absorption function $\sigma(x)$ (see e.g. (2.13) or (2.15)). Therefore, we will only consider the impact from the choice of $\sigma_0 > 0$ on the performance of the PML-II with $R > 0$ fixed in this section.

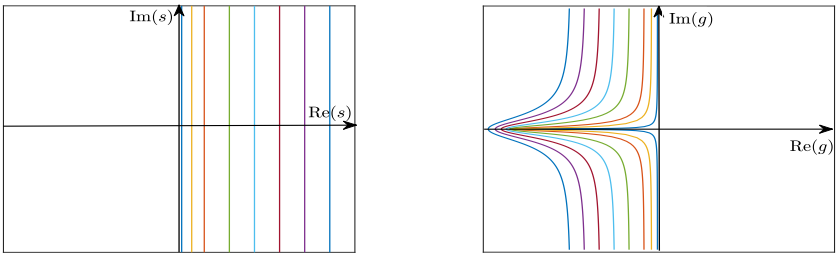

FIGURE 2. The right half complex plane $\mathrm{Re}(s) > 0$ (left) under the mapping $g = -\sqrt{s^2+1}$ (right).

For the numerical discretization of the PML-II formulation (2.8), we use the following direct semi-implicit finite-difference Fourier pseudo-spectral (FD-FP) method:

$$\frac{u^{n+1} - 2u^n + u^{n-1}}{\tau^2} + \frac{A}{2}(u^{n+1} + u^{n-1}) + \frac{1}{2}(u^{n+1} + u^{n-1}) + \lambda(u^n)^3 = 0, \quad n \geq 1, \tag{2.9a}$$

$$u^1 = u_0 + \tau v_0 - \frac{\tau^2}{2}\left[Au_0 + u_0 + \lambda u_0^3\right], \tag{2.9b}$$

where $u^n \in \mathbb{R}^N$ and the matrix

$$A = -d_0 D_1 d_0 D_1, \quad \text{with} \quad d_0 = \mathrm{diag}(1/(1+R\sigma)),$$

and $D_1 \in \mathbb{C}^{N\times N}$ is the matrix representation [38] of the approximate first-order differentiation operator ∂_x in the periodic domain I^*. The time averaging in (2.9a) indeed avoids any CFL type stability condition. The starting value (2.9b) is obtained directly from the Taylor expansion for the three-level scheme (2.9a). Note that (2.9a) reads explicitly

$$u^{n+1} = -u^{n-1} + G^{-1}\left[\frac{2}{\tau^2}u^n - \lambda(u^n)^3\right], \quad n \geq 1, \quad G := \left[\left(\frac{1}{\tau^2} + \frac{1}{2}\right)\mathbb{I} + \frac{1}{2}A\right], \tag{2.10}$$

where $\mathbb{I}$ is the identity matrix in $\mathbb{R}^{N\times N}$. The matrix G^{-1} is dense here, but it can be pre-computed with the chosen τ and N once for all. The computational cost of FD-FP at each time level is therefore $O(N^2)$ if one performs the previous matrix-vector product. However, by borrowing the idea from [10], the scheme (2.10) can be implemented efficiently by incorporating the GMRES

solver with FFT. Here we briefly describe such a strategy for evaluating (2.10). The equation (2.10) equivalently reads

$$\begin{cases} u^{n+1} = -u^{n-1} + w^n, \quad n \geq 1, \\ Gw^n = \dfrac{2}{\tau^2} u^n - \lambda (u^n)^3. \end{cases} \tag{2.11}$$

The second equation of (2.11) can be treated as a linear system with unknown w^n, which can be solved iteratively e.g. by GMRES [37] since it is a matrix-free solver. Within the GMRES iteration, the involved spatial derivatives in G can be straightforwardly implemented by applying the FFT to discretize the operators in the iteration process. The GMRES convergence can be strongly improved by introducing a Fourier diagonalizable preconditioner for $\sigma = 0$, similarly as in [5, 6, 7], i.e.

$$\mathcal{P} G w^n = \mathcal{P} \left[\frac{2}{\tau^2} u^n - \lambda (u^n)^3 \right],$$

with

$$\mathcal{P} = \left(\frac{1}{\tau^2} + \frac{1}{2} - \frac{\partial_{xx}}{2} \right)^{-1}. \tag{2.12}$$

Let us remark that the preconditioning operator $\mathcal{P}$ can also be directly implemented at low cost by FFT, since it has constant coefficients and is therefore diagonalizable. The computational cost of the FD-FP method is then nearly $O(N \log N)$. The global error of FD-FP is similar to EWI-FP, which is $O(\tau^2) + O(h^{m_0})$.

2.3. **Absorption function.** In this subsection, we discuss the choices for the absorption function. To enhance the efficiency of the PMLs, we look for spectral accuracy in the related spatial discretization. Let us recall that getting a smooth absorption function is crucial to get the spectral accuracy, where the parameter $m_0 > 0$ specifies the accuracy induced by the PML absorption function on the error estimates. We shall consider two types of absorption functions $\sigma(x)$ for the PMLs: a classical polynomial choice and a singular function case.

The first possibility is to choose a high degree *polynomial type* function as proposed in [2] for wave equations

$$\sigma_P(x) := \begin{cases} \sigma_0 \left[1 - \left(\dfrac{x - L^*}{\delta} \right)^2 \right]^8, & L \leq |x| \leq L^* = L + \delta, \\ 0, & \text{else.} \end{cases} \tag{2.13}$$

It can be viewed as a smoothed version of the commonly used quadratic or cubic absorbing functions for PMLs [10, 18, 24, 43]. Thanks to the large power, (2.13) is very smooth at the interfaces $|x| = L$ so that one can maintain the high order accuracy from the Fourier spectral discretization in space.

Nevertheless, it is well-known since the work by Bermúdez *et al.* [19, 20, 21] that singular type functions are much more adapted than the polynomial functions for PMLs applied to wave-like equations. More specifically, the σ functions must be such that

$$\int_L^{L^*} \sigma(x) dx = +\infty. \tag{2.14}$$

In particular, they are less subject to parameter tuning problems than in the polynomial case (2.13) to fix the values of σ_0 and δ, in particular thanks to the speed c. This is crucial in our case when prospecting the non-relativistic limit of the NKGE in the next section.

The concrete examples provided by Bermúdez *et al.* do not correspond however to smooth functions, and therefore they lead to a limited accuracy for the pseudo-spectral approach. Here, we propose some simple locally corrected smoother *Bermúdez type* functions as follows: for $k = -1, 0, 1, \ldots$, we define the absorption functions

$$\sigma_{B_k}(x) := \begin{cases} \sigma_0 \beta_k(|x| - L^*), & L \leq |x| \leq L^* = L + \delta, \\ 0, & \text{else,} \end{cases} \tag{2.15}$$

where we set

$$\beta_k(|x|-L^*) = \beta_{-1}(|x|-L^*) - \sum_{j=0}^{k} \frac{1}{j!} \frac{d^j \beta_{-1}(z)}{dz^j}\Big|_{z=-\delta} (|x|-L)^j, \quad \beta_{-1}(z) = -\frac{1}{z}, \quad z \in \mathbb{R}.$$

The function $\sigma_{B_{-1}}$ (i.e. $k=-1$ in (2.15)) is the original absorption function proposed in [19, 20, 21]. It contains both discontinuity and singularity over the domain. For $k \geq 0$ as above, we have introduced a truncated Taylor series expansion of β_{-1} in β_k so that the function $\sigma_{B_k}(x)$ has k-th order continuous derivatives on the interval $|x| < L^*$, which is expected for the spectral scheme.

The polynomial type choice $\sigma(x) = \sigma_P(x)$ is the classical absorption function which is bounded on the whole interval $|x| \leq L + \delta$. Here, $\sigma_0 = \|\sigma_P\|_\infty > 0$ and $\delta > 0$ are known as the *strength* and *thickness* of the PML, respectively. The function σ_P can be directly applied to both PML formulations, i.e. PML-I (2.3) and PML-II (2.8). The Bermúdez type choice $\sigma(x) = \sigma_{B_k}(x)$ has singularities at the two boundary points $|x| = L^*$. The strength of such absorption function can be considered as infinite in some sense. This indeed is a problem for the PML-I formulation (2.3), where in the equations we can see that the infinite function value of $\sigma_{B_k}(x)$ at the boundary is inconsistent with the periodic boundary condition mathematically. Moreover, when the propagating waves are getting close to the boundary, the large values of $\sigma_{B_k}(x)$ near the boundary could make the right-hand-side of the first equation in (2.3) stiff which causes numerical instability problems in schemes like EWI-FP. Thus, for PML-I (2.3), we shall only consider the polynomial absorption function σ_P (2.13). As for the PML-II formulation (2.8), in contrast, $\sigma_{B_k}(x)$ can be directly applied in the equation, where we have a well-defined function $S(x)$ on I^* with zero boundary values, i.e. in (2.8) with $\sigma = \sigma_{B_k}$ for any $k \in \mathbb{N}$,

$$S(x) := \frac{1}{1 + R\sigma_{B_k}(x)}, \quad |x| \leq L^*, \quad \text{where} \quad S(\pm L^*) = 0.$$

Therefore, we shall consider both types of absorption functions for PML-II (2.8).

2.4. **Numerical results.** In this subsection, we conduct some numerical experiments to illustrate the performance of the two presented types of PML formulations as well as the proposed numerical schemes. We shall denote in the following $u = u(x,t)$ as the exact solution of the NKGE (2.1), $u_{\rm pml} = u_{\rm pml}(x,t)$ as the exact solution of the PML-I (2.3) or PML-II (2.8), and $u^n_{\rm pml} \approx u_{\rm pml}(x,t_n)$ as the corresponding numerical solution from EWI-FP (2.6) or FD-FP (2.9).

PML-I. We begin with the PML-I formulation (2.3). Within these tests, we fix the absorption function as the high order polynomial type function (2.13), i.e.

$$\sigma(x) = \sigma_P(x), \quad |x| \leq L^*.$$

First of all, we verify the accuracy of our numerical solver EWI-FP (2.6) for approximating (2.3) with

$$\lambda = 1, \quad u_0 = 5\mathrm{e}^{-x^2}, \quad v_0 = \frac{1}{2}\mathrm{sech}(x^2), \tag{2.16}$$

and fix $\alpha = 0$, $\sigma_0 = 8$, $\delta = 0.5$, $L = 4$ for the layer. Then we compute the relative maximum error

$$e^{n,\infty}_{\rm pml} := \frac{\|u^n_{\rm pml} - u_{\rm pml}\|_{L^\infty(I)}}{\|u_{\rm pml}\|_{L^\infty(I)}} \tag{2.17}$$

on the physical domain $I = (-L, L)$ at some time $t = t_n$, where the reference solution $u_{\rm pml}$ of (2.3) is obtained here numerically by using EWI-FP under a fine mesh with $\tau = 1 \times 10^{-4}$ and $h = 1/128$. The temporal and spatial errors of the EWI-FP scheme (2.6) at $t = 4$ are shown in Figure 3, where we fix $h = 1/32$ for the temporal error (left) and $\tau = 1 \times 10^{-4}$ for the spatial error (right). From the numerical results in Figure 3, we can clearly see that the proposed EWI-FP (2.6) for solving (2.3) with (2.13) converges in time with a second-order accuracy and converges in space with a near spectral accuracy.

Next, we test the error of the PML-I formulation (2.3) for approximating the solution to the NKGE (2.1). We use EWI-FP with a very fine mesh, e.g. $\tau = 1 \times 10^{-4}$ and $h = 1/128$, such that

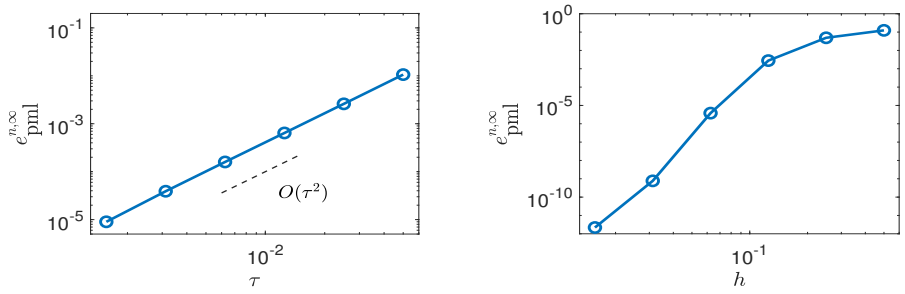

FIGURE 3. The temporal (left) and spatial (right) $e^{n,\infty}_{\rm pml}$-errors of EWI-FP for PML-I.

the numerical discretization error is rather negligible. We compute the following relative PML error as a function of time $t > 0$

$$e^2_{\rm pml}(t) := \frac{\|u(\cdot,t) - u_{\rm pml}(\cdot,t)\|_{L^2(I)}}{\|u(\cdot,t)\|_{L^2(I)}}, \quad I = (-L, L), \tag{2.18}$$

under some different strength σ_0 or thickness δ parameters for the absorption function (2.13). We use the same numerical example (2.16) as above, and we measure the error (2.18) on the physical domain $I = (-4, 4)$. The exact solution $u(x,t)$ of (2.1) is obtained by using the EWI-FP scheme (for u only) to solve (2.1) accurately on a large enough interval, e.g. $(-16, 16)$, where the solution within the computational time is still away from the boundary. The relative errors (2.18) as a function of time under different parameters for (2.13) are plotted in Figure 4. To compare the performance of the PML-I (2.3) in the nonlinear case of the Klein-Gordon equation with its linear case, we also include in Figure 4 the error result (2.18) under the same example (2.16) but with $\lambda = 0$ in (2.1) and (2.3). For (2.16), the profiles of the exact solution of (2.1) and the PML solution of (2.3) at time $t = 4$ and $t = 6$ are reported in Figure 5 for the PML parameters $\sigma_0 = 8$ and $\delta = 7/8$.

From the numerical results in Figures 4 and 5, we can see that the PML-I (2.3) is effectively approximating the solution of NKGE (2.1) within the physical domain (see Figure 5). The PML-I formulation in the linear case, i.e. $\lambda = 0$ in (2.3), was proposed to be perfectly matched for the linear Klein-Gordon equation in [2]. In the nonlinear case, i.e. $\lambda \neq 0$ in NKGE (2.1), although PML-I (2.3) is not theoretically perfectly matched, its performance is very close to the linear case (cf. the first row and the second row in Figure 4). With increasing strength of the absorption function and thickness of the fictitious layer, the accuracy of PML-I could be improved (see Figure 4).

Remark 2.1. With a usual low order polynomial absorption function σ, e.g. the quadratic or cubic polynomial in [10, 18, 24, 43], the performance of the PML-I (2.3) is similar to that in Figure 4. However, the spatial convergence rate of the EWI-FP method would only be at the second- or third-order. These numerical results are omitted here for brevity.

Remark 2.2. The choice of $\alpha \geq 0$ barely impacts the performance of PML-I (2.3), where the PML errors (2.18) when using different α are very close. This is not surprising within the context of the analysis of the damping effect in (2.5). Therefore, we only present the numerical results for $\alpha = 0$.

PML-II. Under the same numerical example (2.16), we present the numerical experiments for PML-II given by (2.8). The physical domain is fixed as $I = (-4, 4)$. For these tests, we will consider both the polynomial choice (2.13) and the Bermúdez type function (2.15) as the absorption function for PML-II.

Firstly, we take the polynomial choice (2.13) as the absorption function, i.e. $\sigma(x) = \sigma_P(x)$ for PML-II. Similarly as before, with $\sigma_0 = 8$ and $\delta = 0.5$ fixed for the absorption function, we first show the temporal and spatial accuracy of the numerical method, i.e. FD-FP (2.9) at $t = 4$ in Figure 6. Next, by taking in FD-FP a very fine mesh ($\tau = 10^{-4}$ and $h = 1/256$) so that the numerical

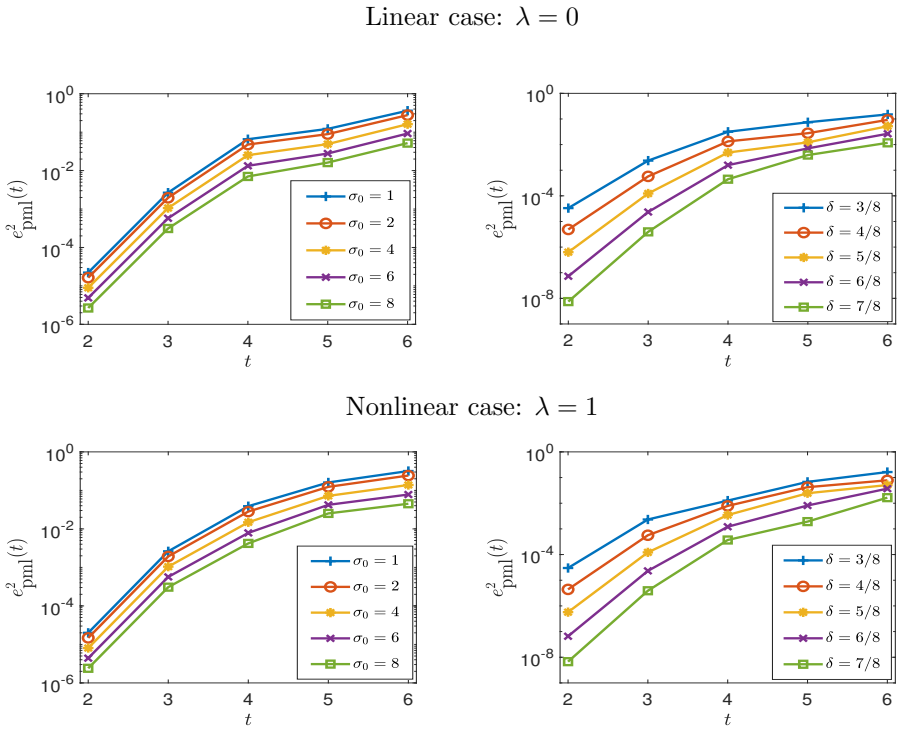

FIGURE 4. The PML-I $e^2_{\rm pml}$-error as a function of time for $\sigma = \sigma_P$ in the linear and nonlinear cases: $\delta = 1/2$ and varying strength σ_0 (left), and $\sigma_0 = 6$ and varying thickness δ (right).

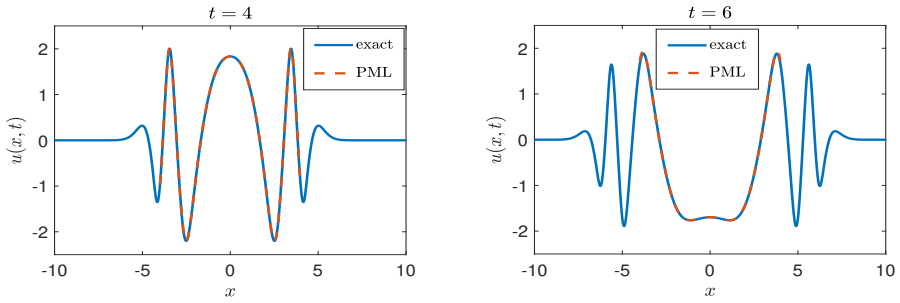

FIGURE 5. The exact solution and the PML-I solution at $t = 4$ (left) and $t = 6$ (right).

discretization error is negligible, the corresponding PML error (2.18) of the PML-II formulation (2.8) is shown in Figure 7 as a function of time for different values of σ_0 and δ (for $R = 1$ in (2.8)).

As explained in Section 2.2 by the dispersion relation in the linear case, the factor R must be positive to avoid any instability. To confirm the formal analysis and illustrate the stability issue in the PML-II equation (2.8) with respect to R, we show in Figure 8 the evolution of the maximum norm of the PML solution $u_{\rm pml}$ of (2.8) for $R > 0$ or $R \in \mathbb{C}$.

From the numerical results in Figures 6-8, we can conclude that:

1) The PML-II formulation (2.8) with $R > 0$ is stable (see Figure 8), while, for R with any non-zero imaginary part, instability will occur in (2.8).

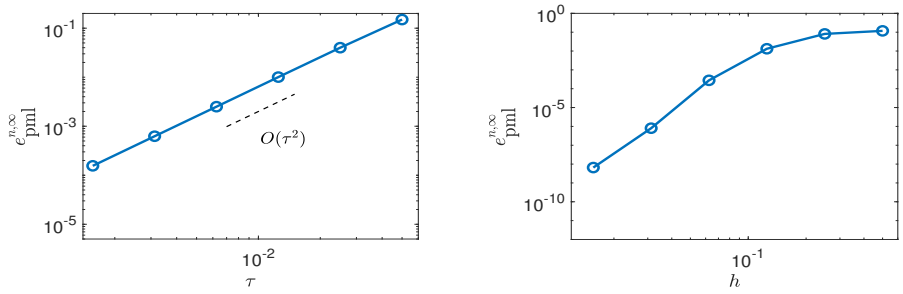

FIGURE 6. The temporal (left) and spatial (right) $e^{n,\infty}_{\rm pml}$-errors of FD-FP for PML-II with $\sigma = \sigma_P$.

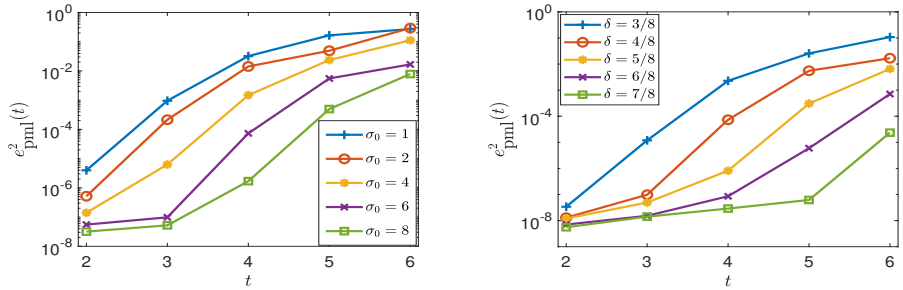

FIGURE 7. The PML-II $e^2_{\rm pml}$-error as a function of time under $\sigma = \sigma_P$: for $\delta = 1/2$ and varying strength σ_0 (left), and for $\sigma_0 = 6$ and varying thickness δ (right).

2) The FD-FP method (2.9) is also second-order accurate in time and nearly spectrally accurate in space. Under the same mesh size and time step, it is slightly less accurate than the EWI-FP method (cf. Figures 6 and 3). Therefore, from the numerical discretization point of view, PML-II is a little bit less efficient than the PML-I.
3) PML-II effectively approximates the exact solution of NKGE (2.1) (see Figure 7). Moreover, under the same absorption function $\sigma(x)$ with the same strength and thickness, the error from the PML-II is smaller than PML-I particularly as time increases (cf. Figures 7 and 4). Therefore, from the modelling truncation point of view, PML-II is more effective than PML-I. We remark that the results of using the usual low order polynomial absorption function for PML-II is similar.

Next, we choose the Bermúdez type function (2.15) as the absorption function, i.e. $\sigma(x) = \sigma_{B_k}(x)$ for PML-II (2.8). We use the same example (2.16) with $\sigma_0 = 8, \delta = 0.5$ in (2.15), and we first test the numerical discretization error of the FD-FP method (2.9) for PML-II (2.8) with $R = 1$. The spatial error at $t = 4$ is presented in Figure 9 under different smoothing orders $k \geq 0$ in the Bermúdez function (2.15). The corresponding temporal error is totally the same as in the previous example with the polynomial choice (2.13), so it is omitted here for brevity. On the other hand, to illustrate the efficiency brought by the preconditioner (2.12) for solving (2.11), we fix in this example $\sigma = \sigma_{B_2}$, $\tau = 0.02$ and consider the GMRES solver for the time step $n = 1$ in (2.11). We show the number of iterations needed by the GMRES solver (without restart) to converge at a threshold $\epsilon > 0$ with or without using the preconditioner (2.12) under different values of h in Table 1. This confirms that the preconditioner leads to a convergence independent of the mesh refinement, which is well-adapted to the pseudo-spectral method. The corresponding PML error (2.18) with respect to time in this example is presented in Figure 10 for different values of the parameters σ_0 and δ.

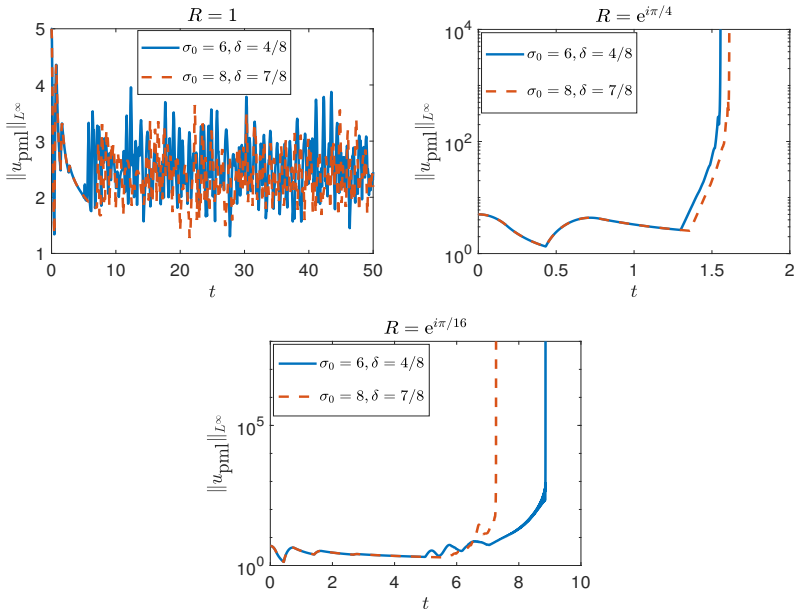

FIGURE 8. Stability of PML-II: $\|u_{\rm pml}\|_{L^\infty}$ as a function of time for $R = 1$ (top left), $R = \mathrm{e}^{i\pi/4}$ (top right), $R = \mathrm{e}^{i\pi/16}$ (bottom).

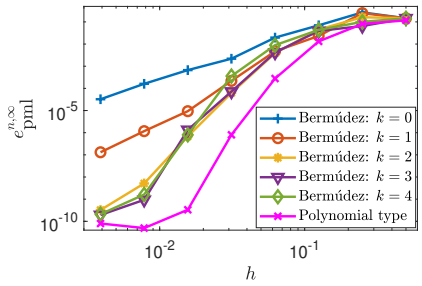

FIGURE 9. Spatial $e^{n,\infty}_{\rm pml}$-error of FD-FP for PML-II with $\sigma = \sigma_{B_k}$, for different values of k.

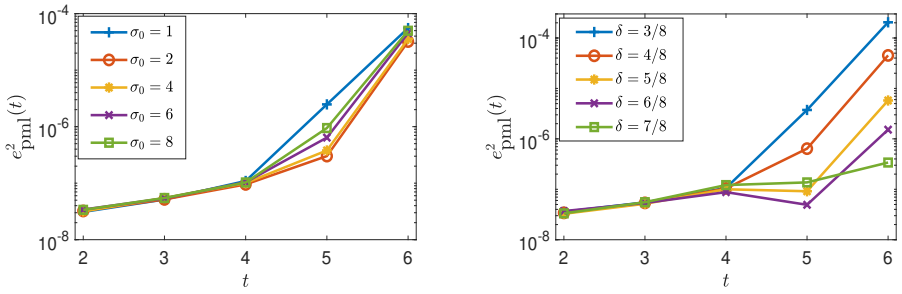

FIGURE 10. The PML-II $e^2_{\rm pml}$-error as a function of time for $\sigma = \sigma_{B_2}$: for $\delta = 1/2$ and varying strength σ_0 (left), and for $\sigma_0 = 6$ and varying thickness δ (right).

TABLE 1. Number of iterations needed by GMRES under threshold ϵ for (2.11) at $n = 1$: with (pre) or without (non) the preconditioner.

$\epsilon = 10^{-10}$	$h = 1/128$	$h = 1/256$	$h = 1/512$	$\epsilon = 10^{-13}$	$h = 1/128$	$h = 1/256$	$h = 1/512$
pre	2	2	2	pre	8	7	7
non	11	20	35	non	24	46	92

Based on the numerical results in Table 1, Figures 9 and 10, we can draw the following observations:

1) For a high enough regularization parameter $k \geq 0$, the spatial error of FD-FP method converges fast. For $k \geq 2$, the Bermúdez function σ_{B_k} is able to offer a near spectral accuracy for the Fourier pseudo-spectral method, although the error is a little bit larger than that for the polynomial choice (2.13) (see Figure 9). Practically, taking $k = 2$ or 3 is enough, since increasing k does not give any more improvements.
2) The proposed GMRES solver (2.11) for FD-FP method works very well with the help of the preconditioner (2.12). The number of iterations needed to reach a threshold has been significantly reduced to $O(1)$ for all mesh sizes. This makes the practical efficiency of the FD-FP method comparable to the EWI-FP method.
3) The PML error of PML-II with Bermúdez function (2.15) is much smaller than that of the polynomial choice (2.13) under the same parameters σ_0 and δ (cf. Figures 10 and 7). Moreover, the accuracy of the PML-II with Bermúdez function is much less sensitive to the choice of the parameters σ_0 and δ (see Figure 10). Therefore, one does not need to tune the parameters for the layer in a practical computation, which makes it suitable for concrete applications and to later investigate the non-relativistic regime of the NKGE.

Energy decay and comparison. To end, we test and compare the energy behaviour of the two PML formulations. We define the following energy functional for some function $w = w(x, t)$

$$H_I(t; w) := \int_I \left[|\partial_t w(x,t)|^2 + |\partial_x w(x,t)|^2 + |w(x,t)|^2 + \frac{\lambda}{2}|w(x,t)|^4 \right] dx, \quad t \geq 0.$$

With the exact solution $w = u$ of (2.1), the above $H_I(t; u)$ denotes the part of the total energy (1.2) inside the physical domain $I = (-L, L)$ for the NKGE (2.1). Note that the quantity $H_I(t; u)$ is not conserved by (2.1), and in fact it should be decaying with respect to time, since the waves in the solution $u(x, t)$ keep propagating to the far field as time evolves.

We take the example (2.16) with $I = (-4, 4)$. For PML-I given by (2.3), we consider $\sigma = \sigma_P$ with $\sigma_0 = 8$, $\delta = 6/8$, $\alpha = 0$. For PML-II as defined by (2.8), we take $\sigma = \sigma_{B_2}$ with $\sigma_0 = 3$, $\delta = 6/8$, $R = 1$. We compute H_I with the exact solution $w = u$ of (2.1), and with the exact solution $w = u_{\text{pml}}$ of PML-I (2.3) or PML-II (2.8). The "exact" solutions here are obtained numerically as before. The numerical results are reported in Figure 11 until the final time $t = 22$. We see that both PML-I and PML-II follow the exact energy decay very well in long time, and the approximation from PML-II is however more accurate than PML-I for all times.

Overall, based on the presented numerical experiments in this section for approximating the NKGE (2.1) in the classical scaling, we suggest to rather use the PML-II formulation (2.8) with the regularized Bermúdez absorption function (2.15) for $k \geq 2$, not only from the point of view of the temporal and spatial accuracy, but also for the stability to fix the tuning parameters of the PML.

3. PML FOR NON-RELATIVISTIC SCALING

Physically when $c \to \infty$, the NKGE (1.1) is said to be in the non-relativistic limit regime [33, 34, 42]. In such a case, it is often convenient to introduce the scaling [13, 35]:

$$x \to \frac{x}{x_s}, \quad t \to \frac{t}{t_s}, \quad \lambda \to \lambda m x_s^2, \quad \text{with} \quad t_s = \frac{m x_s^2}{\hbar}, \quad \varepsilon = \frac{\hbar}{m c x_s},$$

where t_s and x_s are the time and length units, respectively, and $\varepsilon > 0$ is a dimensionless parameter. Then, the formulation of the one-dimensional real-valued case of (1.1) in the non-relativistic scaling

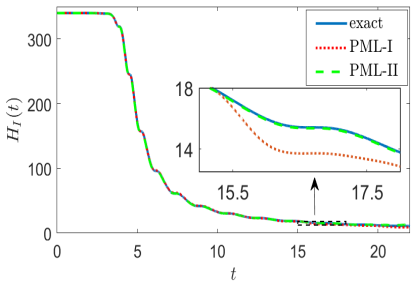

FIGURE 11. Energy decay of the PMLs in physical domain: $H_I(t)$ obtained from PML-I, PML-II and the NKGE.

reads [12, 15, 23]:

$$\begin{cases} \varepsilon^2 \partial_{tt} u(x,t) - \partial_{xx} u(x,t) + \dfrac{1}{\varepsilon^2} u(x,t) + \lambda u(x,t)^3 = 0, \quad t > 0, \ x \in \mathbb{R}, \\ u(x,0) = u_0(x), \quad \partial_t u(x,0) = v_0(x), \quad x \in \mathbb{R}. \end{cases} \tag{3.1}$$

In the following, we shall consider $\varepsilon \in (0,1]$. The NKGE (3.1) in such scaling could describe the physical system where the wave speed is smaller than the speed of light but with non-negligible relativistic effects [15, 35, 42]. It also appears in the high-plasma-frequency limit regime for plasma physics [14, 16]. For $\varepsilon = 1$, (3.1) leads to the classical NKGE (2.1), and as $\varepsilon \to 0$, we are in the non-relativistic limit regime.

3.1. **PML-II.** We adopt the same notations as introduced in the previous section. Now in the same spirit as (2.8), the PML-II in the non-relativistic scaling reads:

$$\begin{cases} \varepsilon^2 \partial_{tt} u - \dfrac{1}{1+R\sigma} \partial_x \left(\dfrac{1}{1+R\sigma} \partial_x u \right) + \dfrac{1}{\varepsilon^2} u + \lambda u^3 = 0, \quad t > 0, \ x \in I^*, \\ u(x,0) = u_0(x), \quad \partial_t u(x,0) = v_0(x), \quad x \in I^*, \\ u(-L^*,t) = u(L^*,t), \quad t \geq 0. \end{cases} \tag{3.2}$$

For the linear case of (3.2), i.e. $\lambda = 0$, let us now consider a plane wave solution: $u(x,t) = \mathrm{e}^{i(kx-\omega t)}$ with $k, \omega \in \mathbb{R}$ satisfying the dispersion relation:

$$\omega = \pm \frac{\sqrt{1+\varepsilon^2 k^2}}{\varepsilon^2},$$

which provides the phase velocity

$$v_p = \frac{\omega}{k} = \pm \frac{\sqrt{k^{-2}+\varepsilon^2}}{\varepsilon^2}.$$

From the above, it is clear to see that waves with all wavelengths are travelling to infinity at the speed $O(\varepsilon^{-2})$ as $\varepsilon \to 0$. Therefore, when ε is small, the waves in (3.1) enter and pass through the damping layer $L \leq |x| \leq L + \delta$ very quickly, and then get reflected at the opposite outer boundary $|x| = L + \delta$ because of the periodic boundary conditions. This fact may leave the layer not enough time to effectively absorb all the waves. In fact, we will show later by numerical tests, for a fixed PML setup under the classical polynomial absorption function (2.13), i.e. fixed σ, δ, R as ε decreases, that the PML-II (3.2) will soon fail to approximate the exact solution of NKGE in the physical domain.

In order to get a stable absorber with rather uniform damping effect for $\varepsilon \in (0,1]$, we will verify later by numerical experiments that we need to choose

$$R = R^\varepsilon = O(1/\varepsilon^2) \in \mathbb{R}^+, \quad \text{if} \quad \sigma(x) = \sigma_P(x), \tag{3.3}$$

for the PML-II (3.2) with fixed $\sigma_P(x)$. This is clearly equivalent to say that with $R > 0$ fixed as $\varepsilon \to 0$, we need to choose the strength of the absorption (2.13) $\sigma_0 = O(\varepsilon^{-2})$. Based on the studies from the previous section, we know that the accuracy of the Bermúdez absorption function (2.15) is not very sensitive to the choice of the strength parameter σ_0. Therefore, it is hopeful and reasonable that with the Bermúdez's absorption function in the PML-II (3.2), the damping effect is rather uniform for $\varepsilon \in (0, 1]$ by using

$$R = O(1) \in \mathbb{R}^+, \quad \text{if} \quad \sigma(x) = \sigma_{B_k}(x).$$

It is well-known that as $\varepsilon \to 0$, the solution of the NKGE (3.1) contains rapid oscillations in time [15, 33, 34, 39]:

$$u(x,t) = \mathrm{e}^{it/\varepsilon^2} z(x,t) + \mathrm{e}^{-it/\varepsilon^2} \overline{z}(x,t) + O(\varepsilon^2), \quad t \geq 0, \ x \in \mathbb{R}, \tag{3.4}$$

where $z = z(x,t)$ solves a nonlinear Schrödinger equation independent of ε. In space, the solution u of NKGE (3.1) is rather smooth with wavelength independent of ε. As an illustrative example, we take

$$u_0 = 5\mathrm{e}^{-x^2}, \quad v_0 = \frac{1}{2}\mathrm{sech}(x^2), \quad \lambda = \frac{1}{2}, \tag{3.5}$$

and we show the profile of the exact solution $u(x,t)$ at $t = 4$ in the physical domain $x \in (-4.5, -4)$ under different ε in Figure 12. While in the PML-II formulation (3.2), due to the fast reflected waves (or the incoming waves due to the periodic boundary condition), the ε-dependent oscillations will be induced to the space variable x of the solution. To see this, we consider in (3.2) the physical domain $I = (-4, 4)$ with the layer setup $\sigma_0 = 3$, $\delta = 0.5$, $R = \varepsilon^{-2}$ in σ_P (2.13), and we show in Figure 12 the PML solution $u_{\rm pml}(x,t)$ of (3.2) at $t = 4$ inside the layer $-L - \delta \leq x \leq -L$. The PML solution $u_{\rm pml}(x,t)$ under the same parameters values but with $R = 1$ and σ_{B_2} (2.15) is also given in Figure 12. It can be seen from Figure 12 that, as ε decreases, the PML solution $u_{\rm pml}(x,t)$ exhibits more and more spatial oscillations inside the layer. Such phenomenon will cause numerical difficulties to the spatial discretization of the PML-II formulation (3.2). As we shall report in the numerical tests, the accuracy of the Fourier pseudo-spectral discretization for (3.2) depends on ε.

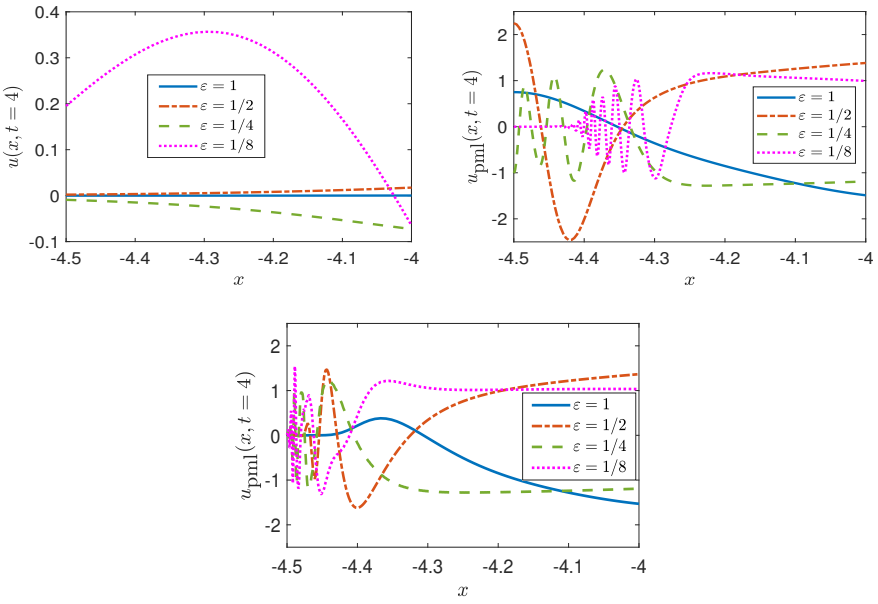

FIGURE 12. Profiles of the exact solution $u(x,t)$ of NKGE (top left) and the PML-II solution $u_{\rm pml}(x,t)$ with $R = \varepsilon^{-2}$ and $\sigma = \sigma_P$ (top right), or with $R = 1$ and $\sigma = \sigma_{B_2}$ (bottom).

For the FD-FP method, the finite-difference discretization of (3.2) with $R = R^\varepsilon$ directly reads:

$$\varepsilon^2 \frac{u^{n+1} - 2u^n + u^{n-1}}{\tau^2} + \frac{A^\varepsilon}{2}(u^{n+1} + u^{n-1}) + \frac{1}{2\varepsilon^2}(u^{n+1} + u^{n-1}) + \lambda(u^n)^3 = 0,$$

which gives the FD-FP scheme

$$u^{n+1} = -u^{n-1} + (G^\varepsilon)^{-1} \left[\frac{2\varepsilon^2}{\tau^2} u^n - \lambda(u^n)^3 \right], \quad n \geq 1, \tag{3.6}$$

with

$$G^\varepsilon = \left[\left(\frac{\varepsilon^2}{\tau^2} + \frac{1}{2\varepsilon^2} \right) \mathbb{I} + \frac{1}{2} A^\varepsilon \right], \quad A^\varepsilon = -d_0 D_1 d_0 D_1, \quad d_0 = \mathrm{diag}(1/(1 + R^\varepsilon \sigma)).$$

For the above matrix G^ε that depends on ε in the scheme, we will show later by numerical results that its condition number remains small and stays uniformly bounded as $\varepsilon \to 0$. Similarly as (2.10), it can also be implemented efficiently by the GMRES solver with a preconditioner in the non-relativistic scaling:

$$\begin{cases} u^{n+1} = -u^{n-1} + w^n, \quad n \geq 1, \\ \mathcal{P}^\varepsilon G^\varepsilon w^n = \mathcal{P}^\varepsilon \left[\dfrac{2\varepsilon^2}{\tau^2} u^n - \lambda(u^n)^3 \right], \end{cases} \qquad \mathcal{P}^\varepsilon = \left(\frac{\varepsilon^2}{\tau^2} + \frac{1}{2\varepsilon^2} - \frac{\partial_{xx}}{2} \right)^{-1}. \tag{3.7}$$

The starting value for (3.6) if directly using the construction from the Taylor expansion reads

$$u^1 = u_0 + \tau v_0 - \frac{\tau^2}{2\varepsilon^2} \left[A^\varepsilon u_0 + \frac{u_0}{\varepsilon^2} + \lambda u_0^3 \right],$$

where the $O(1/\varepsilon^2)$ and $O(1/\varepsilon^4)$ terms in the above will induce instability to the scheme, since $u^1 = O(1/\varepsilon^4)$ could be very large for small ε. To avoid this, we consider a filtered data:

$$u^1 = u_0 + \tau v_0 - \frac{\tau}{2} \sin(\tau/\varepsilon^2) \left[A^\varepsilon u_0 + \lambda u_0^3 \right] - \frac{\tau}{2} \sin(\tau/\varepsilon^4) u_0, \tag{3.8}$$

so that $u^1 = O(1)$.

Thanks to the filtered starting value (3.8) as well as the time averaging, the FD-FP method (3.6) is stable for all $\varepsilon \in (0, 1]$. This means that we have the boundedness of the numerical solution of FD-FP up to a fixed time if $\tau \leq C$ for some $C > 0$ independent of ε or the spatial mesh size h. However, owning to the ε-dependent oscillation frequencies in both time and space directions of the PML solution of (3.2), it is expected that the FD-FP method (2.9) is not uniformly accurate for approximating (3.2) as $\varepsilon \to 0$. One then needs to use mesh sizes $\tau > 0$ and $h > 0$ that depend on ε to reach the same accuracy level at a fixed time.

Remark 3.1. It is beyond the scope of this paper to investigate whether the asymptotic expansion (3.4) also holds for the PML-II equation (3.2) or not. If it is still valid, then formally as $\varepsilon \to 0$, the PML-II (3.2) is consistent with the limit: a nonlinear Schrödinger equation with PML presented in [9, 43]. We shall address this question in a future study.

3.2. **PML-I.** Next, we consider the PML-I formulation under the non-relativistic scaling. To write the correct ε-dependent PML model for (3.1), we shall proceed the derivation as in [2].

We begin by considering a linear case of (3.1):

$$\varepsilon^2 \partial_{tt} u - \partial_{xx} u + \frac{1}{\varepsilon^2} u + \lambda u = 0. \tag{3.9}$$

By taking the Laplace transform on both sides of the above equation, we get

$$\left(\varepsilon^2 s^2 - \partial_{xx} + \frac{1}{\varepsilon^2} + \lambda \right) \widehat{u}(x, s) = 0, \quad \widehat{u}(x, s) = \int_0^\infty u(x, t) \mathrm{e}^{-st} dt,$$

where s is the Laplace variable. By (2.2), we find formally, for some $\alpha \geq 0$ and absorption function $\sigma(x)$,

$$\left(\varepsilon^2 s^2 + \frac{1}{\varepsilon^2} + \lambda \right) \widehat{u} = \frac{s + \alpha}{s + \alpha + \sigma} \partial_x \left(1 - \frac{\sigma}{s + \alpha + \sigma} \right) \partial_x \widehat{u}. \tag{3.10}$$

Let

$$\widehat{\eta}_1 = -\frac{1}{s+\alpha+\sigma}\partial_x \widehat{u},$$

then from (3.10) we have

$$\varepsilon^2\left(s^2+s\sigma\right)\widehat{u} - \varepsilon^2\sigma\alpha\widehat{u} + \sigma\frac{\varepsilon^2\alpha^2}{s+\alpha}\widehat{u} = \partial_x\left(\partial_x\widehat{u}+\sigma\widehat{\eta}_1\right) - \left(\frac{1}{\varepsilon^2}+\lambda\right)\widehat{u} - \sigma\frac{\varepsilon^{-2}+\lambda}{s+\alpha}\widehat{u}.$$

By taking the inverse Laplace transform of the above equation and further letting

$$\widehat{\eta}_2 = -\frac{\varepsilon^2\alpha^2+\varepsilon^{-2}+\lambda}{s+\alpha}\widehat{u},$$

we obtain

$$\begin{aligned}
&\varepsilon^2\partial_{tt}u - \partial_{xx}u + \frac{1}{\varepsilon^2}u + \lambda u = \partial_x(\sigma\eta_1) + \varepsilon^2\sigma\alpha u - \varepsilon^2\sigma\partial_t u + \sigma\eta_2,\\
&\partial_t\eta_1 + (\alpha+\sigma)\eta_1 + \partial_x u = 0, \quad \partial_t\eta_2 + \alpha\eta_2 + \left(\varepsilon^2\alpha^2+\frac{1}{\varepsilon^2}\right)u + \lambda u = 0,
\end{aligned}$$

which is a PML system for the linear model problem (3.9). To proceed from the linear case to the nonlinear case, as proposed in [2], we directly replace the term λu by λu^3 in the above expressions. Then together with the domain truncation similarly as (2.3), the PML-I formulation for NKGE (3.1) in the non-relativistic scaling reads

$$\begin{cases}
\varepsilon^2\partial_{tt}u - \partial_{xx}u + \dfrac{1}{\varepsilon^2}u + \lambda u^3 = \sigma\left(\eta_2 + \varepsilon^2\alpha u - \varepsilon^2\partial_t u\right) + \partial_x(\sigma\eta_1), \quad t>0,\ x\in I^*,\\
\partial_t\eta_1 + (\alpha+\sigma)\eta_1 + \partial_x u = 0,\\
\partial_t\eta_2 + \alpha\eta_2 + \left(\varepsilon^2\alpha^2+\dfrac{1}{\varepsilon^2}\right)u + \lambda u^3 = 0,\\
u(x,0) = u_0(x), \quad \partial_t u(x,0) = v_0(x), \quad \eta_1(x,0) = \eta_2(x,0) = 0, \quad x\in I^*,\\
u(-L^*,t) = u(L^*,t), \quad \eta_1(-L^*,t) = \eta_1(L^*,t), \quad \eta_2(-L^*,t) = \eta_2(L^*,t), \quad t\geq 0.
\end{cases} \tag{3.11}$$

Asymptotically, the limit of the PML-I system (3.11) as $\varepsilon\to 0$ is not clear. It can be seen from (3.11) that there is a $O(\varepsilon^{-2})$ term in the equation of η_2, which acts as a very stiff source term as $0<\varepsilon\ll 1$. Numerically, to propose a stable and accurate numerical algorithm for solving (3.11) is a challenge for small ε. In this paper, we do not intend to address this issue, and we shall focus on the investigation of the two PML formulations and the two choices of absorption functions. In the following, let us simply apply the EWI-FP discretization from Section 2.1.

The EWI-FP method for (3.11) then reads: for $n\geq 0$,

$$u^{n+1} = \cos(\langle\partial_x\rangle_\varepsilon\tau)u^n + \frac{\sin(\langle\partial_x\rangle_\varepsilon\tau)}{\langle\partial_x\rangle_\varepsilon}v^n + \frac{\tau\sin(\langle\partial_x\rangle_\varepsilon\tau)}{2\varepsilon^2\langle\partial_x\rangle_\varepsilon}f^n, \tag{3.12a}$$

$$\eta_1^{n+1} = \mathrm{e}^{-(\sigma+\alpha)\tau}\eta_1^n - \frac{\tau}{2}\left[\mathrm{e}^{-(\sigma+\alpha)\tau}\partial_x u^n + \partial_x u^{n+1}\right], \tag{3.12b}$$

$$\eta_2^{n+1} = \mathrm{e}^{-\alpha\tau}\eta_2^n - \frac{\tau}{2}\left[\mathrm{e}^{-\alpha\tau}\left((\varepsilon^2\alpha^2+\varepsilon^{-2})u^n + \lambda(u^n)^3\right) + (\varepsilon^2\alpha^2+\varepsilon^{-2})u^{n+1} + \lambda(u^{n+1})^3\right], \tag{3.12c}$$

$$v^{n+1} = -\langle\partial_x\rangle_\varepsilon\sin(\langle\partial_x\rangle_\varepsilon\tau)u^n + \cos(\langle\partial_x\rangle_\varepsilon\tau)v^n + \frac{\tau}{2\varepsilon^2}\left[\cos(\langle\partial_x\rangle_\varepsilon\tau)f^n + f^{n+1}\right], \tag{3.12d}$$

with

$$\langle\partial_x\rangle_\varepsilon = \frac{\sqrt{1-\varepsilon^2\partial_{xx}}}{\varepsilon^2}, \quad f^n = \sigma\left(\eta_2^n - \varepsilon^2 v^n + \varepsilon^2\alpha u^n\right) + \partial_x(\sigma\eta_1^n) - \lambda(u^n)^3.$$

As we discussed in the previous section, for each fixed ε, the EWI-FP has a CFL as $\tau < Ch$. Now, the scheme is much more constrained since for each fixed h as $\varepsilon\to 0$, the EWI-FP scheme (3.12) has a severe stability constraint: $\tau\lesssim\varepsilon^2$, due to the stiffness that we mentioned above. Moreover, we are not able to directly apply the Bermúdez absorption function in (3.12) due to the singularity in σ_{B_k} (2.15) and stability issue. So, we have to consider the classical choice (2.13) for (3.11) or (3.12) and tune the parameters for every ε. Concerning these drawbacks, we recommend to rather use the PML-II formulation (3.2) than PML-I (3.11) for NKGE in the non-relativistic scaling.

3.3. **Numerical results.** In this subsection, we present the numerical results for the above two PML formulations for the NKGE in the non-relativistic scaling. Let us take the given data in (3.5) for the NKGE (3.1) in the following tests. We begin with the numerical investigations of PML-II, and we shall consider similarly as before its performance under the two kinds of absorption functions, and finally analyze shortly PML-I.

PML-II with polynomial type absorption function. We start with the *polynomial type* absorption function $\sigma(x) = \sigma_P(x)$ as (2.13) for the PML-II (3.2). First of all, we illustrate the performance of the PML-II formulation (3.2) with (2.13) under different choices of the parameter $R > 0$. We measure the error (2.18) on the physical domain $I = (-4, 4)$ by choosing

$$R = 1, \quad \text{or} \quad R = 1/\varepsilon, \quad \text{or} \quad R = 1/\varepsilon^2,$$

with $\sigma_0 = 3$ fixed and some values of the layer thickness δ. We show in Figure 13 the error (2.18) of the PML-II (3.2) for approximating (3.1) at $t = 4$ under different ε, where the last choice is clearly the most accurate.

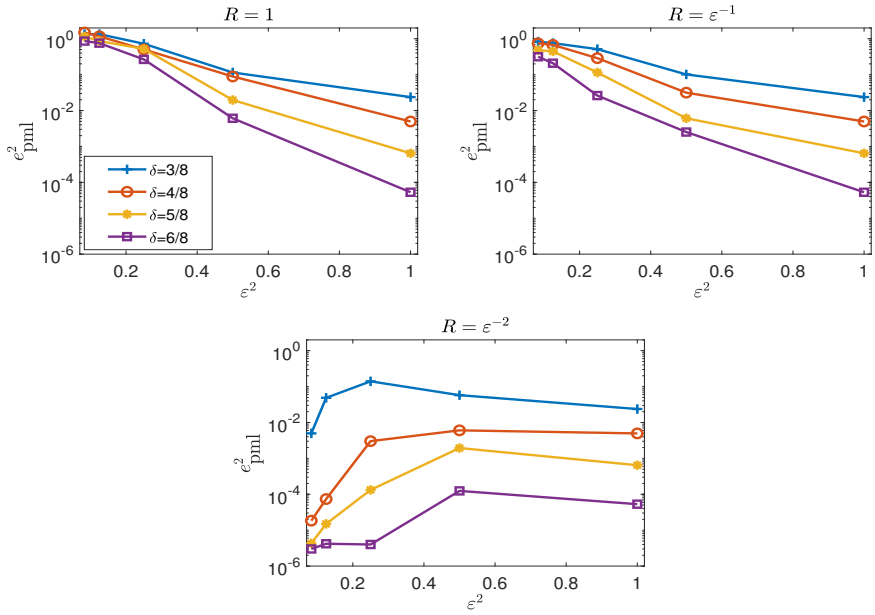

FIGURE 13. PML-II $e^2_{\rm pml}$-error with respect to ε for fixed $\sigma_0 = 3$ and different parameter values δ: $\sigma = \sigma_P$ with strategy $R = 1$ (top left), $R = \varepsilon^{-1}$ (top right) and $R = \varepsilon^{-2}$ (bottom).

Next, we test the performance of the FD-FP method (3.6) for approximating the PML-II formulation (3.2) for different ε under the choice $R = R^\varepsilon = 1/\varepsilon^2$. In these tests, we fix $\sigma_0 = 3$ and $\delta = 4/8$ for the layer. The reference solution is obtained by using the FD-FP method with a very fine mesh, e.g. $\tau = 10^{-4}$, $h = 1/2048$ for each ε. The temporal and spatial errors (2.17) of the FD-FP method under different ε at $t = 4$ are shown in Figure 14. Moreover, by taking $\tau = 10^{-4}$, $h = 1/128$ as mesh sizes in this test, we show in Figure 15 the condition number (in spectral norm) of the iterative matrix G^ε as a function of ε for the FD-FP method (3.6).

Based on the numerical results in Figures 13-15, we can conclude on the following observations for the PML-II formulation and the FD-FP method with polynomial type absorption function σ_P:

1) With the strategy $R = 1/\varepsilon^2$, the accuracy of the PML-II is uniform with respect to ε as far as we could test. In contrast, if one takes $R = 1$ or $R = 1/\varepsilon$, the error of PML-II increases dramatically as ε decreases (see Figure 13). Overall, when ε is small, the accuracy of PML-II

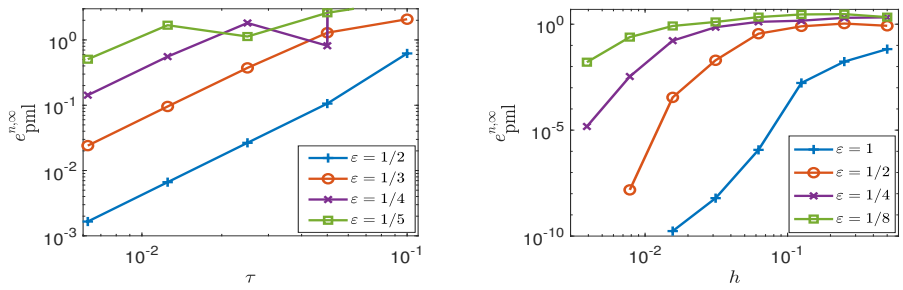

FIGURE 14. Temporal (left) and spatial (right) accuracy of FD-FP: $e^{n,\infty}_{\rm pml}$-error for $\sigma = \sigma_P$ with different ε.

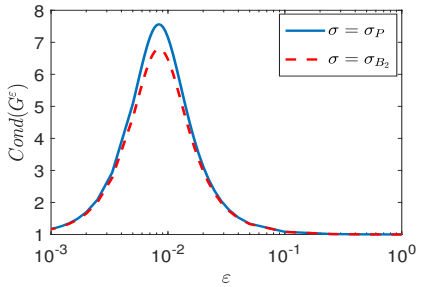

FIGURE 15. The condition number of the iterative matrix G^ε of FD-FP for PML-II: polynomial case $\sigma = \sigma_P$ and Bermúdez type $\sigma = \sigma_{B_2}$.

with σ_P is much more sensitive than for the classical scaling case to the parameters R or saying equivalently the strength $R\sigma_0$ and the layer size δ.

2) For $0 < \varepsilon \leq 1$, the condition number of the iterative matrix G^ε in the FD-FP scheme (3.6) stays uniformly bounded and small (see Figure 15), so the linear system in (3.6) can be solved accurately and efficiently. For each fixed ε, we still have the second-order temporal accuracy and the near spectral accuracy in space for the FD-FP method (see Figure 14). When ε decreases with fixed mesh size τ and h, the approximation error of FD-FP in both time and space increases quickly. The ε-dependence of the temporal accuracy is due to the $O(\varepsilon^{-2})$ oscillation frequency in time, and the spatial accuracy is affected by the fast reflections at the boundary of the layer as we explained before. A future goal is therefore to construct a numerical algorithm that is uniformly accurate for $0 < \varepsilon \leq 1$, which would certainly make the PML more efficient.

PML-II with Bermúdez type absorption function. Let us consider $\sigma(x) = \sigma_{B_k}(x)$ as defined in (2.15) for the PML-II (3.2). To test the PML error, we take the PML-II (3.2) with $\sigma = \sigma_{B_2}$, i.e. $k = 2$ in (2.15), for $\sigma_0 = 3$ fixed. By using some different values of $R > 0$ and $\delta > 0$, we show in Figure 16 the PML approximation error (2.18) on the physical domain $I = (-4, 4)$ at $t = 4$. With $\sigma = \sigma_{B_2}$, $R = 1$, $\delta = 4/8$, we plot in Figure 17 the numerical discretization error (2.17) of the FD-FP method at $t = 4$ in time and in space. Under $\tau = 10^{-4}$, $h = 1/128$, the corresponding condition number of the matrix G^ε as a function of ε is also shown in Figure 15. The number of iterations needed for the convergence of GMRES (for threshold $\epsilon = 10^{-10}$ without restart) with the preconditioner (3.7) for solving (3.6) at $n = 1$ under $\tau = 0.02$, $\delta = 3/8$, $R = 1$ is given in Figure 18 (left) for different $\varepsilon > 0$ and values of h. The number of iterations needed for solving (3.6) under $\tau = 2 \times 10^{-4}$, $h = 1/128$, $\delta = 3/8$, $R = 1$ until time $t = 6$ is given in Figure 18 (right). Let us remark that, without this preconditioner, the iterative solver may not converge when ε gets smaller.

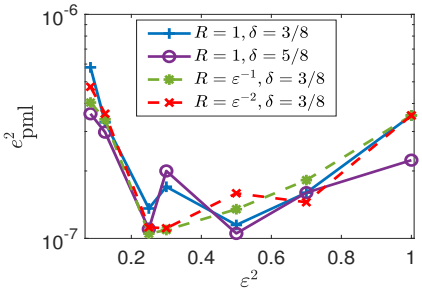

FIGURE 16. PML-II $e^2_{\rm pml}$-error with respect to ε for fixed $\sigma_0 = 3$ and different δ or R for $\sigma = \sigma_{B_2}$.

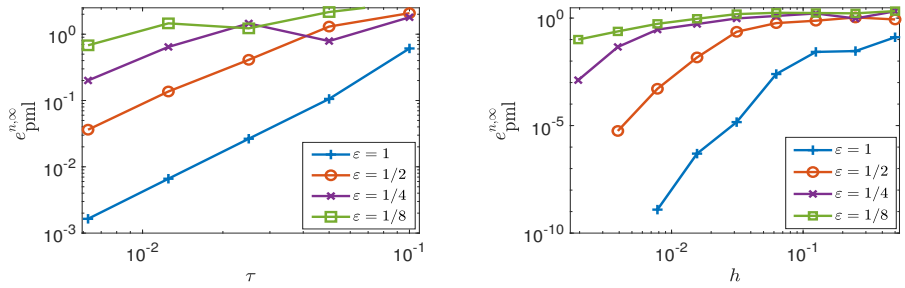

FIGURE 17. Temporal (left) and spatial (right) accuracy of FD-FP: $e^{n,\infty}_{\rm pml}$-error for $\sigma = \sigma_{B_2}$ with different ε.

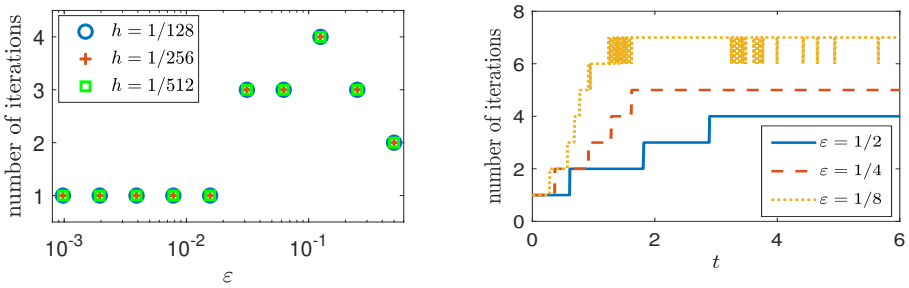

FIGURE 18. Number of iterations needed by GMRES (fixed threshold $\epsilon = 10^{-10}$) with the preconditioner for (3.6) at $n = 1$ (left) and for (3.6) until $t = 6$ (right).

It can be seen from Figures 16-18 that

1) The numerical discretization error of the FD-FP method for PML-II (3.2) with the Bermúdez absorption function (2.15) is close to the case of the polynomial choice above (cf. Figures 14 and 17). The temporal and spatial error grows dramatically as ε decreases, but with τ, $h \to 0$, the FD-FP method still converges and the condition number of G^ε is again uniformly bounded for $0 < \varepsilon \leq 1$. The preconditioner (3.7) still works very well for $0 < \varepsilon < 1$, which improves significantly the efficiency of the GMRES solver, since it exhibits a convergence rate independent of the mesh refinement h. Moreover, the number of iterations stays small and bounded in time, and is relatively insensitive to ε.

2) The PML-II (3.2) with the Bermúdez absorption function (2.15) is much more accurate than that of the classical polynomial choice (2.13) (cf. Figures 16 and 13). With the Bermúdez function, the PML-II is still not sensitive to the parameters for the layer, i.e. R, σ_0, δ. More importantly, the error appears to be rather uniform with respect to $\varepsilon \in (0, 1]$ as far as we could test. Thus, we can simply take fixed R, σ_0, $\delta = O(1)$ for all $\varepsilon \in (0, 1]$. While, we remark that for smaller ε, it is getting harder to eliminate the impact from the numerical error of the FD-FP solver due to error behaviour observed in Figure 17.

Tests for PML-I. At last, we report some numerical results for the PML-I formulation (3.11) when approximating the NKGE (3.1) and illustrate its drawbacks compared with PML-II (3.2). We use the same numerical example (3.5) and take $\alpha = 0$ in (3.11). The PML error (2.18) of the PML-I formulation (3.11) at $t = 4$ with respect to ε is given in Figure 19 under $\sigma_0 = 8$ and different parameter values δ. It is clear from the numerical results in Figure 19 that the PML-I formulation (3.11) with the classical absorption function (2.13) is very sensitive to the parameters: σ_0, δ and ε. When ε becomes small, the error of PML-I is much larger than that of the PML-II (cf. Figure 19 and Figures 13 and 16). In particular, for small values of ε, the accuracy of PML-I can barely be improved by increasing δ. One must keep enlarging the strength parameter σ_0, while the stiffness brought by large σ in (3.11) will consequently increase the difficulty for the numerical solver.

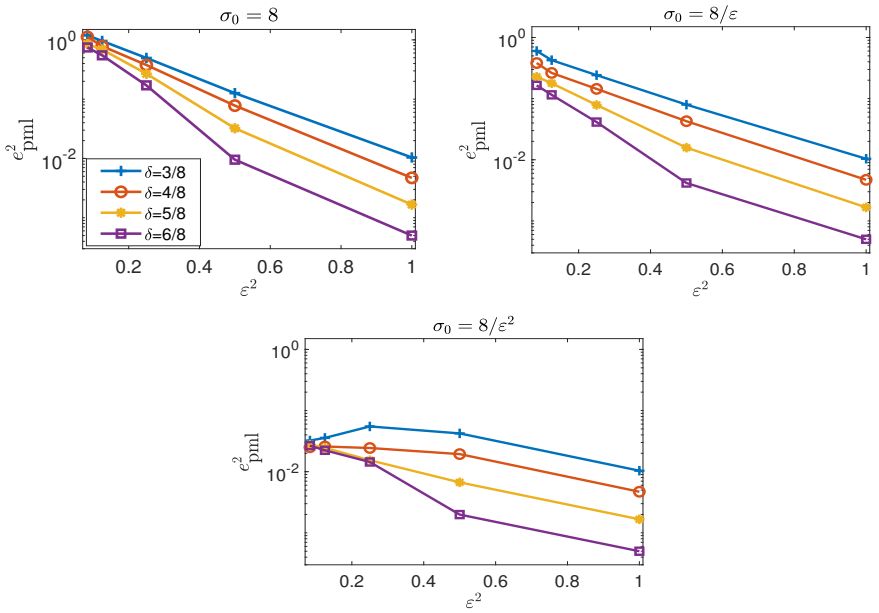

FIGURE 19. PML-I e^2_{pml}-error with respect to ε for different δ: $\sigma_0 = 8$ (top left), $\sigma_0 = 8/\varepsilon$ (top right) and $\sigma_0 = 8/\varepsilon^2$ (bottom).

4. Extension to the 2D rotating NKGE

In this section, we shall apply the PML-II formulation to simulate the vortices dynamics in a two-dimensional rotating NKG model. The rotating NKGE has been introduced to model the dynamics of the cosmic superfluid in a rotating frame, and in two space dimensions it reads [35, 42]:

$$\partial_{tt}\Psi - \Delta\Psi + \Psi + \lambda|\Psi|^2\Psi - 2i\Omega L_z\partial_t\Psi - \Omega^2 L_z^2\Psi = 0, \quad \mathbf{x} = (x, y)^\intercal \in \mathbb{R}^2, \ t > 0,$$
$$\Psi(\mathbf{x}, 0) = \psi_0(\mathbf{x}), \quad \partial_t\Psi(\mathbf{x}, 0) = \psi_1(\mathbf{x}), \quad \mathbf{x} \in \mathbb{R}^2,$$

where the solution $\Psi = \Psi(\mathbf{x}, t)$ is a complex-valued scalar field, $\Omega > 0$ is the given angular velocity and $L_z = -i(x\partial_y - y\partial_x)$ is the angular momentum operator. As proposed in [35], by introducing

the rotating matrix

$$A(t) := \begin{pmatrix} \cos(\Omega t) & \sin(\Omega t) \\ -\sin(\Omega t) & \cos(\Omega t) \end{pmatrix}, \quad t \geq 0,$$

and a change of variable to the *rotating Lagrangian coordinates*:

$$u(\tilde{\mathbf{x}}, t) = \Psi(\mathbf{x}, t), \quad \mathbf{x} = A(t)\tilde{\mathbf{x}},$$

the two angular momentum terms can be eliminated and the model becomes the NKGE (removing the $\tilde{}$ for conciseness) [35]:

$$\begin{cases} \partial_{tt} u(\mathbf{x}, t) - \Delta u(\mathbf{x}, t) + u(\mathbf{x}, t) + \lambda |u(\mathbf{x}, t)|^2 u(\mathbf{x}, t) = 0, \quad \mathbf{x} \in \mathbb{R}^2, \ t > 0, \\ u(\mathbf{x}, 0) = \psi_0(\mathbf{x}), \quad \partial_t u(\mathbf{x}, 0) = \Omega \nabla \psi_0(\mathbf{x}) \cdot \begin{pmatrix} y \\ -x \end{pmatrix} + \psi_1(\mathbf{x}), \quad \mathbf{x} \in \mathbb{R}^2. \end{cases} \tag{4.1}$$

Then, we can directly extend the PML-II formulation to the above initial value problem which leads to

$$\begin{cases} \partial_{tt} u(\mathbf{x}, t) - \dfrac{1}{1 + R\sigma(x)} \partial_x \left(\dfrac{1}{1 + R\sigma(x)} \partial_x u(\mathbf{x}, t) \right) - \dfrac{1}{1 + R\sigma(y)} \partial_y \left(\dfrac{1}{1 + R\sigma(y)} \partial_y u(\mathbf{x}, t) \right) \\ \qquad + u(\mathbf{x}, t) + \lambda |u(\mathbf{x}, t)|^2 u(\mathbf{x}, t) = 0, \quad t > 0, \ \mathbf{x} \in I^* = (-L^*, L^*)^2, \\ u(\mathbf{x}, 0) = \psi_0(\mathbf{x}), \quad \partial_t u(\mathbf{x}, 0) = \Omega \nabla \psi_0(\mathbf{x}) \cdot \begin{pmatrix} y \\ -x \end{pmatrix} + \psi_1(\mathbf{x}), \quad \mathbf{x} \in I^*, \\ u(-L^*, y, t) = u(L^*, y, t), \quad t \geq 0, \quad y \in [-L^*, L^*], \\ u(x, -L^*, t) = u(x, L^*, t), \quad t \geq 0, \quad x \in [-L^*, L^*], \end{cases} \tag{4.2}$$

where $L^* = L + \delta$. With

$$S_x = -\frac{1}{1 + R\sigma(x)} \partial_x \left(\frac{1}{1 + R\sigma(x)} \partial_x \right), \quad S_y = -\frac{1}{1 + R\sigma(y)} \partial_y \left(\frac{1}{1 + R\sigma(y)} \partial_y \right),$$

for short, the finite-difference time discretization for (4.2) then reads

$$\frac{u^{n+1} - 2u^n + u^{n-1}}{\tau^2} + \frac{S_x + S_y}{2}(u^{n+1} + u^{n-1}) + \frac{1}{2}(u^{n+1} + u^{n-1}) + \lambda |u^n|^2 u^n = 0, \quad n \geq 1,$$

$$u^1 = u_0 + \tau v_0 - \frac{\tau^2}{2} \left[(S_x + S_y) u_0 + u_0 + \lambda |u_0|^2 u_0 \right],$$

where $u^n = u^n(\mathbf{x}) \approx u(\mathbf{x}, t)$ for $n \geq 1$ and $u_0 = u(\mathbf{x}, 0)$, $v_0 = \partial_t u(\mathbf{x}, 0)$. By applying the Fourier pseudo-spectral discretization in the x- and y-directions to the equations, we obtain the FD-FP scheme. By further incorporating the previous equations with the preconditioned GMRES and FFT in 2D, we can implement the FD-FP scheme in the same manner as before:

$$\begin{cases} u^{n+1} = -u^{n-1} + w^n, \quad n \geq 1, \\ \mathcal{P} G w^n = \mathcal{P} \left[\dfrac{2}{\tau^2} u^n - \lambda |u^n|^2 u^n \right], \end{cases}$$

where

$$G = \left[\left(\frac{1}{\tau^2} + \frac{1}{2} \right) \mathbb{I} + \frac{S_x + S_y}{2} \right], \quad \mathcal{P} = \left(\frac{1}{\tau^2} + \frac{1}{2} - \frac{\partial_{xx}}{2} - \frac{\partial_{yy}}{2} \right)^{-1}.$$

To illustrate the accuracy of the PML-II approach, we consider the following example. We take in (4.2) the parameters

$$L = 4, \quad \lambda = 3, \quad \Omega = 2, \quad R = 1,$$

and four initially separated vortices

$$\psi_0(\mathbf{x}) = \psi_1(\mathbf{x}) = (x - c_0 + iy)(x + c_0 + iy)(x + i(y - c_0))(x + i(y + c_0)) \mathrm{e}^{-(x^2 + y^2)/2},$$

with $c_0 = 1.32$. The profile of the initial data for the NKGE is shown in Figure 20.

We use the Bermúdez function $\sigma = \sigma_{B_2}$ (2.15) as the absorption function and choose $\sigma_0 = 3$ and $\delta = 0.5$. By applying the FD-FP similarly as in Section 2.2, we solve the PML equation (4.2) accurately and look at the solution u_{pml} on the physical domain $I = (-L, L)^2$. As a reference solution, we solve (4.1) directly on the sufficiently large domain $(-16, 16)^2$ and compare the exact

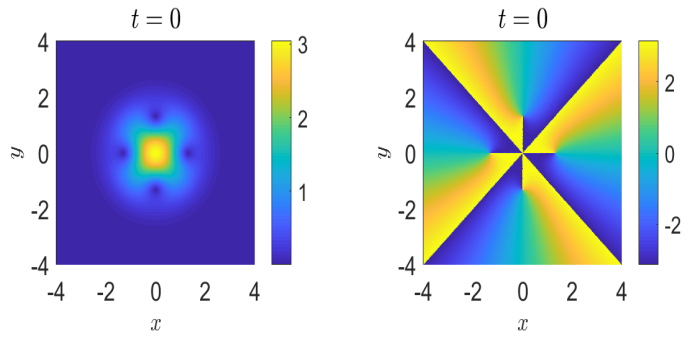

FIGURE 20. Contour plot of the initial data: $|\psi_0(\mathbf{x})|$ (left) and $\mathrm{Arg}(\psi_0(\mathbf{x}))$ (right) for (4.1) or (4.2).

solution u with the PML solution. The dynamics of the exact solution $u(\mathbf{x}, t)$ and the PML solution $u_{\mathrm{pml}}(\mathbf{x}, t)$ are shown on the domain I in Figure 21. The corresponding trajectory of the decaying energy $H_I(t; w)$:

$$H_I(t; w) := \int_I \left[|\partial_t w(x,t)|^2 + |\nabla w(x,t)|^2 + |w(x,t)|^2 + \frac{\lambda}{2}|w(x,t)|^4 \right] dx, \quad t \geq 0,$$

with $w = u$ or u_{pml} is reported in Figure 22. For both the solution and the energy, we see an excellent agreement between both solutions that cannot be reached when using standard periodic boundary conditions, unless taking a huge spatial domain.

5. Conclusion

In this work, we investigated numerically two kinds of PML formulations for approximating the nonlinear Klein-Gordon equation: a first-order formulation borrowed from the study for general wave equations (PML-I), and a second-order formulation proposed as analogy for the Helmholtz and nonlinear Schrödinger equations (PML-II). For both PML formulations, we developed efficient and accurate pseudo-spectral schemes for the numerical discretizations: i) a pseudo-spectral exponential integrator scheme for PML-I and ii) a linearly implicit preconditioned pseudo-spectral finite-difference scheme for PML-II. To obtain a spectral accuracy, the PML absorption functions were locally regularized. For the NKGE in classical scaling, the PML-II with smoothed Bermúdez type absorption functions and the resulting pseudo-spectral finite-difference scheme are proved to be the most accurate and efficient, owning to the observation that it is less subject to the parameter tuning problems for the layer. Such advantage also distinguishes PML-II for approximating NKGE in the non-relativistic scaling, where the PML solution is found to be not sensitive to the small parameter ε arising in the non-relativistic limit regime. We also extend the method to the accurate computation of vortex dynamics for a rotating NKGE.

Acknowledgements

Research conducted within the context of the Sino-French International Associated Laboratory for Applied Mathematics - LIASFMA. X. Antoine thanks the LIASFMA funding support of the Université de Lorraine. X. Zhao is partially supported by the Natural Science Foundation of Hubei Province No. 2019CFA007 and the NSFC 11901440.

References

[1] D. Appelö, T. Hagstrom, G. Kreiss, Perfectly matched layers for hyperbolic systems: general formulation, well-posedness, and stability, SIAM J. Appl. Math. 67 (2006), pp. 1-23.

[2] D. Appelö, G. Kreiss, Application of a perfectly matched layer to the nonlinear wave equation, Wave Motion 44 (2007), pp. 531-548.

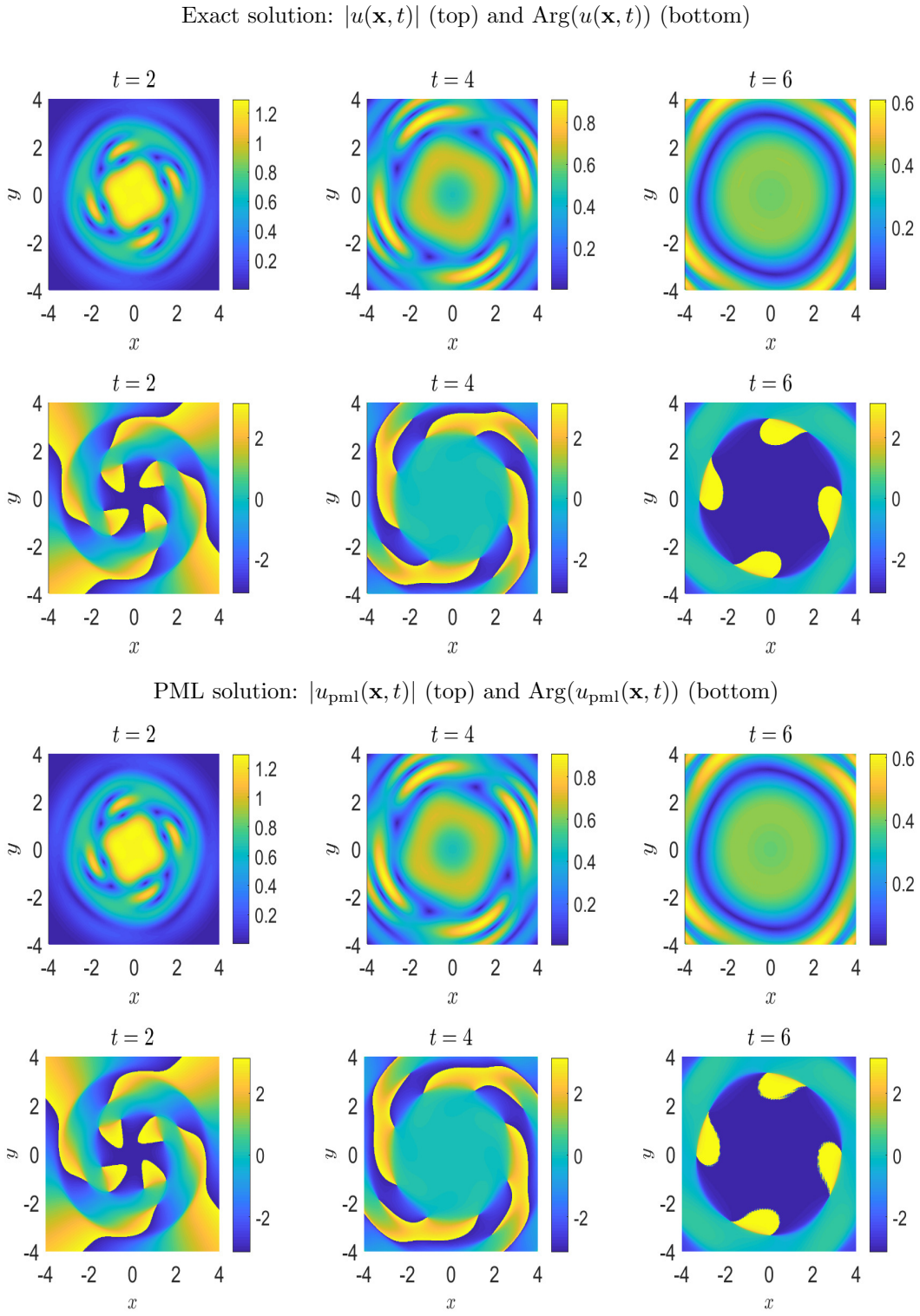

FIGURE 21. Contour plots of exact solution $|u(\mathbf{x},t)|$ and $\mathrm{Arg}(u(\mathbf{x},t))$ of (4.1) and the PML solution $|u_{\mathrm{pml}}(\mathbf{x},t)|$ and $\mathrm{Arg}(u_{\mathrm{pml}}(\mathbf{x},t))$ of (4.2) at times $t=2,4,6$ on the domain I.

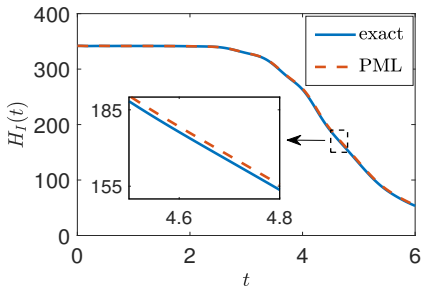

FIGURE 22. The energy decay of the 2D example: $H_I(t)$ with respect to time.

[3] X. ANTOINE, A. ARNOLD, C. BESSE, M. EHRHARDT, A. SCHÄDLE, A review of transparent and artificial boundary conditions techniques for linear and nonlinear Schrödinger equations, Commun. Comput. Phys. 4 (2008), pp.729-796.

[4] X. ANTOINE, W. BAO AND C. BESSE, Computational methods for the dynamics of nonlinear Schrödinger and Gross-Pitaevskii equations, (A Feature Article) Comput. Phys. Commun. 184 (2013), pp. 2621-2633.

[5] X. ANTOINE, R. DUBOSCQ, Robust and efficient preconditioned Krylov spectral solvers for computing the ground states of fast rotating and strongly interacting Bose-Einstein condensates, J. Comput. Phys. 258 (2014), pp.509-523.

[6] X. ANTOINE, R. DUBOSCQ, GPELab, a Matlab toolbox to solve Gross-Pitaevskii equations I: computation of stationary solutions, Comput. Phys. Commun. 185 (2014), pp. 2969-2991.

[7] X. ANTOINE, R. DUBOSCQ, GPELab, a Matlab toolbox to solve Gross-Pitaevskii equations II: dynamics and stochastic simulations, Comput. Phys. Commun. 193 (2015), pp. 95-117.

[8] X. ANTOINE AND R. DUBOSCQ, Modeling and computation of Bose-Einstein Condensates: stationary states, nucleation, dynamics, stochasticity, in Nonlinear Optical and Atomic Systems: at the Interface of Mathematics and Physics, Lecture Notes in Mathematics, 2146, pp. 49-145, Springer, 2015.

[9] X. ANTOINE, E. LORIN, Q. TANG, A friendly review of absorbing boundary conditions and perfectly matched layers for classical and relativistic quantum waves equations, Molecular Physics 115 (2017), pp. 1861-1879.

[10] X. ANTOINE, C. GEUZAINE, Q. TANG, Perfectly matched layer for computing the dynamics of nonlinear Schrödinger equations by pseudospectral methods. Application to rotating Bose-Einstein condensates, Commun. Nonlinear Sci. Numer. Simulat. 90 (2020), pp. 105406.

[11] W. BAO, Y. CAI, Mathematical theory and numerical methods for Bose-Einstein condensation, Kinet. Relat. Mod. 6 (2013), pp. 1-135.

[12] W. BAO, Y. CAI, X. ZHAO, A uniformly accurate multiscale time integrator pseudospectral method for the Klein–Gordon equation in the nonrelativistic limit regime, SIAM J. Numer. Anal. 52 (2014), pp. 2488-2511.

[13] W. BAO, X. DONG, Analysis and comparison of numerical methods for the Klein-Gordon equation in the nonrelativistic limit regime, Numer. Math. 120 (2012), pp. 189-229.

[14] W. BAO, X. DONG, X. ZHAO, An exponential wave integrator sine pseudospectral method for the Klein–Gordon–Zakharov system, SIAM J. Sci. Comput. 35 (2013), A2903-A2927.

[15] W. BAO, X. ZHAO, Comparison of numerical methods for the nonlinear Klein-Gordon equation in the nonrelativistic limit regime, J. Comput. Phys. 398 (2019), pp. 108886.

[16] W. BAO, X. ZHAO, A uniformly accurate multiscale time integrator spectral method for the Klein-Gordon-Zakharov system in the high-plasma-frequency limit regime, J. Comput. Phys. 327 (2016), pp. 270-293.

[17] G. BAO, H. WU, Convergence analysis of the perfectly matched layer problems for time-harmonic Maxwell's equations, SIAM J. Numer. Anal. 43 (2005), pp. 2121–2143.

[18] J.P. BÉRENGER, A perfectly matched layer for the absorption of electromagnetic waves, J. Comput. Phys. 114 (1994), pp. 185-200.

[19] A. BERMÚDEZ, L. HERVELLA-NIETO, A. PRIETO, R. RODRÍGUEZ, An exact bounded PML for the Helmholtz equation, C. R. Acad. Sci. Paris, Ser. I 339 (2004), pp. 803-808.

[20] A. BERMÚDEZ, L. HERVELLA-NIETO, A. PRIETO, R. RODRÍGUEZ, An optimal perfectly matched layer with unbounded absorbing function for time-harmonic acoustic scattering problems, J. Comput. Phys. 223 (2007), pp. 469-488.

[21] A. BERMÚDEZ, L. HERVELLA-NIETO, A. PRIETO, R. RODRÍGUEZ, An exact bounded perfectly matched layer for time-harmonic scattering problems, SIAM J. Sci. Comput. 30 (2007), pp. 312-338.

[22] D.D. BĂINOV, E. MINCHEV, Nonexistence of global solutions of the initial-boundary value problem for the nonlinear Klein-Gordon equation, J. Math. Phys. 36 (1995), pp.756-762.

[23] PH. CHARTIER, N. CROUSEILLES, M. LEMOU, AND F. MÉHATS, Uniformly accurate numerical schemes for highly oscillatory Klein-Gordon and nonlinear Schrödinger equations, Numer. Math. 129 (2015), pp. 211-250.

[24] F. Collino, P. Monk, The perfectly matched layer in curvilinear coordinates, SIAM J. Sci. Comput. 19 (1998), pp. 2061-2090.
[25] Z.M. Chen, H.J. Wu, An adaptive finite element method with perfectly matched absorbing layers for the wave scattering by periodic structures, SIAM J. Numer. Anal. 41 (2003), pp. 799–826.
[26] A.S. Davydov, Quantum Mechanics, 2nd Edition. Pergamon Press 1976.
[27] X Dong, Z Xu, X Zhao, On time-splitting pseudospectral discretization for nonlinear Klein-Gordon equation in nonrelativistic limit regime, Commun. Comput. Phys. 16 (2014), pp. 440-466.
[28] J. Ginibre, G. Velo, The global Cauchy problem for the nonlinear Klein-Gordon equation-II, Ann. Inst. Henri Poincaré 6 (1989), pp. 15-35.
[29] T. Hagstrom, Perfectly matched layers for hyperbolic systems with applications to the linearized Euler equations, in: Cohen et al. (Ed.), Mathematical and Numerical Aspects of Wave Propagation, Proceedings of the Waves 2003, Springer Verlag, 2003, pp. 125-129.
[30] M. Hochbruck, A. Ostermann, Exponential integrators, Acta Numer. 19 (2010), pp. 209-286.
[31] F.Q. Hu, X.D. Li, D.K. Lin, Absorbing boundary conditions for nonlinear Euler and Navier–Stokes equations based on the perfectly matched layer technique, J. Comput. Phys. 227 (2008), pp. 4398-4424.
[32] S. Johnson, Notes on Perfectly Matched Layers (PMLs), Tech. report, MIT, 2010.
[33] S. Machihara, K. Nakanishi, T. Ozawa, Nonrelativistic limit in the energy space for nonlinear Klein-Gordon equations, Math. Ann. 322 (2002), pp. 603-621.
[34] N. Masmoudi, K. Nakanishi, From nonlinear Klein-Gordon equation to a system of coupled nonlinear Schrödinger equations, Math. Ann. 324 (2002), pp. 359-389.
[35] N. Mauser, Y. Zhang, X. Zhao, On the rotating nonlinear Klein-Gordon equation: non-relativistic limit and numerical methods, Multiscale Model. Simul. 18 (2020), pp. 999-1024.
[36] P.J. Pascual, S. Jiménez, L. Vázquez, Numerical simulations of a nonlinear Klein-Gordon model. Applications. Computational Physics (Granada, 1994). Lecture Notes in Physics, vol. 448. pp. 211-270. Springer, Berlin (1995).
[37] Y. Saad, Iterative Methods for Sparse Linear Systems, 2nd ed. SIAM, 2003.
[38] J. Shen, T. Tang, L. Wang, Spectral Methods: Algorithms, Analysis and Applications, Springer, 2011.
[39] K. Schratz, X. Zhao, On the comparison of asymptotic expansion techniques for the nonlinear Klein-Gordon equation in the nonrelativistic limit regime, Discrete Contin. Dyn. Syst. Ser. B 25 (2020), pp. 2841-2865.
[40] X.F. Sun, Z.H. Jiang, X.W. Hu, G. Zhuang, J.F. Jiang, W.X. Guo, Perfectly matched layer absorbing boundary condition for nonlinear two-fluid plasma equations, J. Comput. Phys. 286 (2015), pp. 128-142.
[41] S. Weinberg, The Quantum Theory of Fields, Volume 1: Foundations. Cambridge University Press, 1995.
[42] C. Xiong, M. Good, Y. Guo, X. Liu, K. Huang, Relativistic superfluidity and vorticity from the nonlinear Klein-Gordon equation, Phys. Rev. D 90 (2014), pp. 125019.
[43] C. Zheng, A perfectly matched layer approach to the nonlinear Schrödinger wave equations, J. Comput. Phys. 227 (2007), pp. 537-556.

X. Antoine: Université de Lorraine, CNRS, Inria, IECL, F-54000 Nancy, France.
Email address: xavier.antoine@univ-lorraine.fr

X. Zhao: School of Mathematics and Statistics & Computational Sciences Hubei Key Laboratory, Wuhan University, 430072 Wuhan, China
Email address: matzhxf@whu.edu.cn